Sensor and Simulation Notes
Note 322
February 20, 1990

Low Voltage Experiments Concerning a Section of a Pulser Array Near the Air-Earth Interface

Y. G. Chen, S. Lloyd, and R. Crumley
Maxwell Laboratories Inc., San Diego, CA

Carl E. Baum
Weapons Laboratory

D. V. Giri
Pro-Tech, 125 University Avenue, Berkeley, CA

Abstract

Reference [1] by the authors addressed a general electromagnetic problem of simulating a distributed source at the air-earth interface by an array of pulsers. The pulsers can be arranged in an in-line or staggered configuration. Some considerations in getting from the switch gaps in pulsers to the interface, by suitably shaped conductors, were also discussed in [1]. However, to be beyond the approximation, carefully designed experimental optimization of the sizes and shapes of these conductors was appropriate. Low voltage experiments were performed with a section of a pulser array and representative experimental results are reported in this note.

FOREWORD

The authors are thankful to Mr. W. Walton, Mr. D. Craig and Lt. J. Crissey of Weapons Laboratory, who have provided encouragement and support at various stages of this effort. Thanks are also due to Mr. G. Barton and Mr. P. Elliott of Maxwell Laboratories, Inc., for their assistance.

CONTENTS

1. Introduction

The authors had considered a general electromagnetic (EM) problem of simulating a distributed sheet source near the air-earth interface in a previous note [1]. Possible applications for such a source include nuclear EMP [2], geological prospecting and detection of buried objects such as underground tunnels. Certain aspects of such sheet sources have been considered theoretically in earlier works [3 to 9], for different applications.

The sheet source at a height h above the air-earth interface is, in practice, realized by a two dimensional array of transient pulse generators. The pulse generators themselves may be viewed as "point" sources at their switch gaps. Consequently, optimally shaped conducting surfaces are required in order to go from the switch gaps to the source or aperture plane. The optimization of these conducting surfaces involve many electromagnetic as well as practical design considerations. The EM considerations include 1) Brewster angle wave launcher, ii) impedance of unit cell and iii) impedance of the transition. These have been discussed in [1]. The geometry of a unit-cell in its top and side views are shown in figure 1. This geometry is suggested by the use of Brewster-angle concept, in order to minimize the early time (or equivalently, the high frequency) reflections from the interface back to the pulser. The unit cell has dimensions $2a' \times 2b'$ or $a \times b$. In an ideal case of plane wave incidence on an interface, there is a unique value of the Brewster angle (at high frequencies), but in the present practical case, there is a variation in Brewster angle corresponding to variation in α as indicated in figure 1. One may conclude that certain optimization of the shaping of the conductor between the switch gap and the interface is essential for this reason. Experiments have been initially performed with a 2:1 ratio (i.e., $w = a = 2b$, rectangular) and also a 1:1 ratio (i.e., $w = b$ and $a = 2w$, square). We have used a single pulser or a unit test cell in the above two sets of experiments. Once the experimental optimization for a unit test cell is achieved, we have also looked at a 3×3 (9 pulsers) array, experimentally. All of these experiments are performed at low voltages ensuring adequate signal to noise ratios in the measurement. The following sections describe the experimental configurations and report the test results.

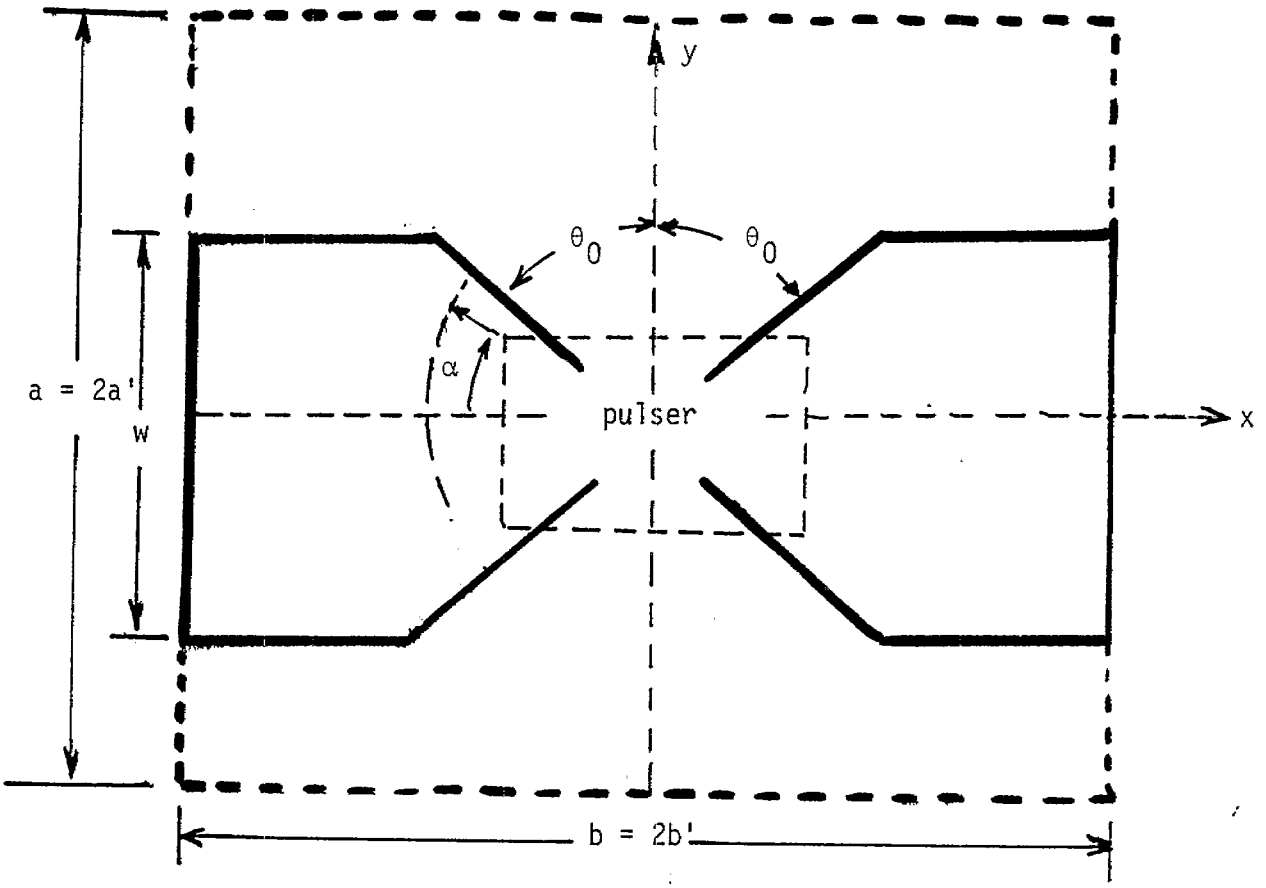

(a) Top view

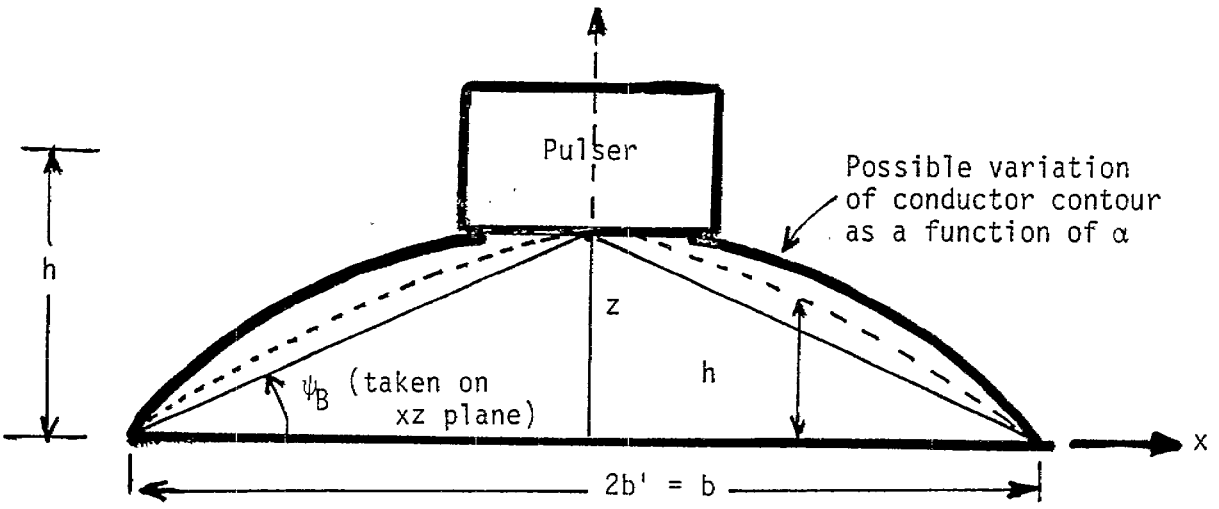

(b) Side view

Figure 1. Geometry of a unit cell in a two dimensional array of pulsers near the air-earth interface.

2. Description of Experimental Configurations

In this section, we briefly outline the experimental configurations. Additional details of the various components of the experimental tests may be found in the Appendix.

The experiments employ fast-rising pulsers driving fields into a plywood test cell, which measures 6m in width, 3m in length and 2m in depth as shown in figure 2. Our present interest lies in investigating the early time or high frequency performance. Consequently, 2m depth of the soil medium, which roughly leads to a clear time of 40 ns is adequate for studying and optimizing the early-time performance. The inside surface of the 6m × 2m sides are lined with aluminum to enhance the physical extant of the sand medium filling the cell. Three conduits, run up the end of the cell opposite the screen box employed in the measurement. The conduits carry the cables from the pulser to the rails. Rails are the conductors that go from the switch gap to aluminum angles at the interface. The cable in the conduit has its center conductor terminated in a matching network shown schematically in figure 3. The 2Ω resistor imulates a "switch gap" and R is chosen so that (R+2)Ω matches the impedance of the driving cable which is typically 50Ω.

Three separate experimental condigurations have been designed in this optimization procedure. They are 1) 2:1 model of a unit cell, 2) 1:1 model of a unit cell and 3) 3 × 3 (9 pulsers array). The ratios 2:1 and 1:1 refer to the ratio of w to b in figure 1a. The first two configurations, i.e., 2:1 and 1:1 models of unit cell are described in this section and the 3 × 3 array of an optimized unit cell is dealt with in the following Section 3.

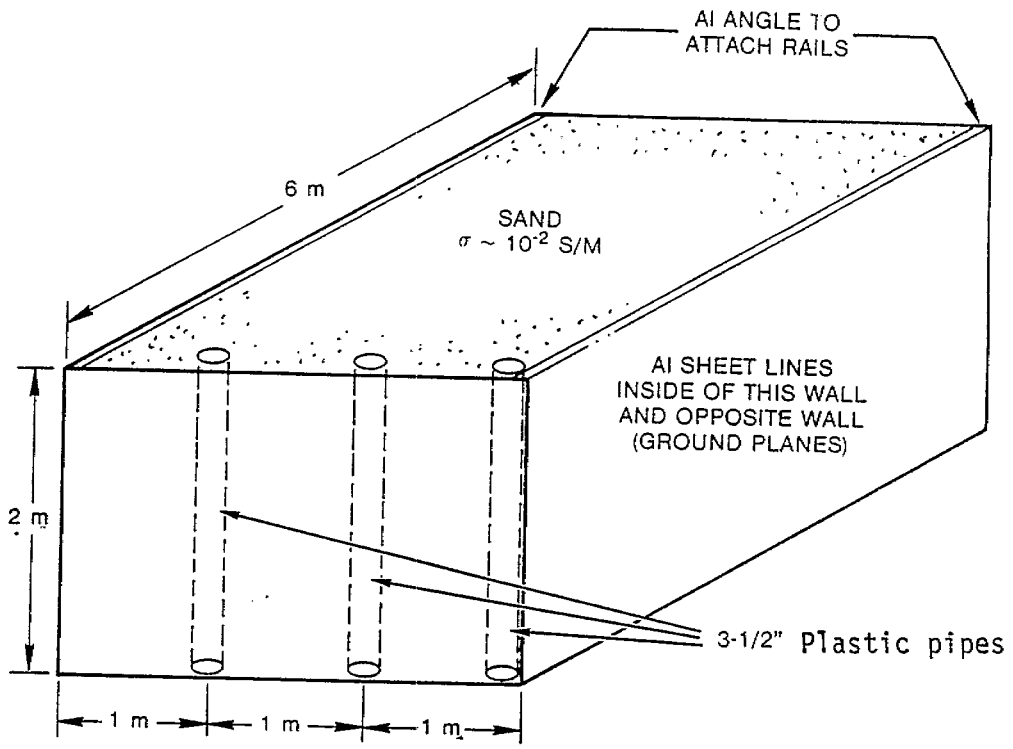

Figure 2. Plywood test cell filled with sand.

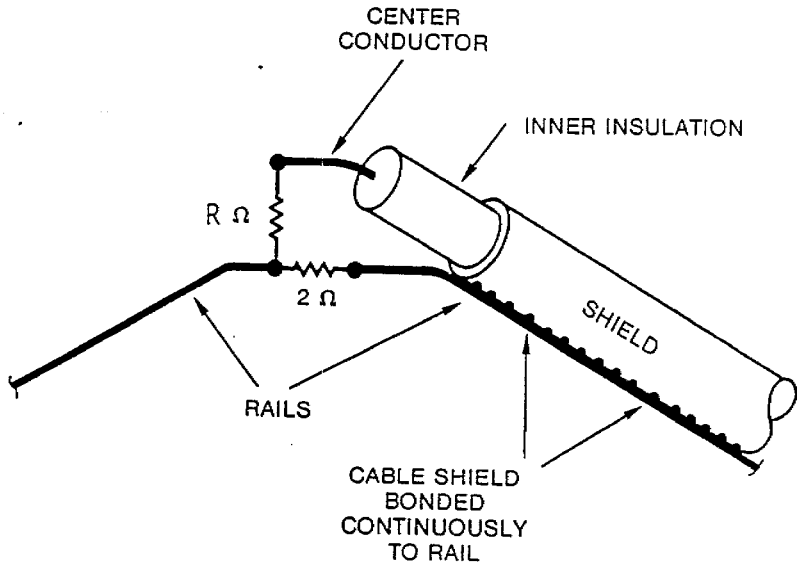

Figure 3. The matching network in driving the nails

3. Low Voltage Experimental Test Results

A. 2:1 (width to length ratio) model

A series of tests were conducted to optimize the energy transfer characteristics of a 2:1 (i.e., w = a = 6m and b = 3m in figure 1a) model into a unit cell of size 6m × 3m. The plywood sandbox of figure 2 is 6m × 3m in dimension and represents a unit cell size. The model (2:1) under investigation is shown in figure 4. The dimensions of the unit cell is 6m × 3m and w is seen to be equal to a (= 6m) and twice b, with b = 3m. The rails are driven by: a) Tektronix 109 pulse generator, b) Maxwell 40151 pulser (50 KV amplitude and $\leq$ 10 ns rise) and c) a 100 KV amplitude source with $\leq$ 10 ns rise time. The rail shape and size optimization was done by the use of a TDR. The angle ψ_B is 17°, corresponding to the Brewster angle for a soil ε_r = 10.

When driven by Tektronix 109 pulser or the Maxwell 40151 pulser, the magnetic field is monitored at 4 locations A, B, C and D shown in figure 5 by the use of an MGL-6A(A) sensor. The two signals from the sensor are transported on two bonded equal length of RG-401 cables to a screen box on the other side of the plywood sandbox and recorded as (A-(-B)). With the Maxwell 40151 pulse, adequate signal strength was available for passive integration. When a Tecktronix 109 was used a a source, B-dot was recorded and B(t) obtained via digitization and numerical or software integration, due to small signal strengths. In addition to the fidelity of the wave shapes produced, a rise time figure of merit or maximum rate of rise τ_e defined below is used.

$$\tau_e = B_{peak}/\dot{B}_{peak} \qquad (1)$$

τ_e is used in judging the fast portion of the measured waveforms while using (1) in practice, since the peak of the integrated waveform was always not attainable, a fairly late time value at t = 12 ns was used consistently.

Initially, TDR measurements were used to optimize the impedance matching. The general features of a TDR measurement are shown in figure 6. The experimental objective is to optimize the TDR measurement by varying the shape of the rails, which are "butterfly" like conducting surfaces. The rail optimization consisted of the following steps during the experiments. The initial angles are θ_0 = 1.6° and ψ_B = 17° [1], for an assumed relative dielectric constant of 10 for the soil medium.

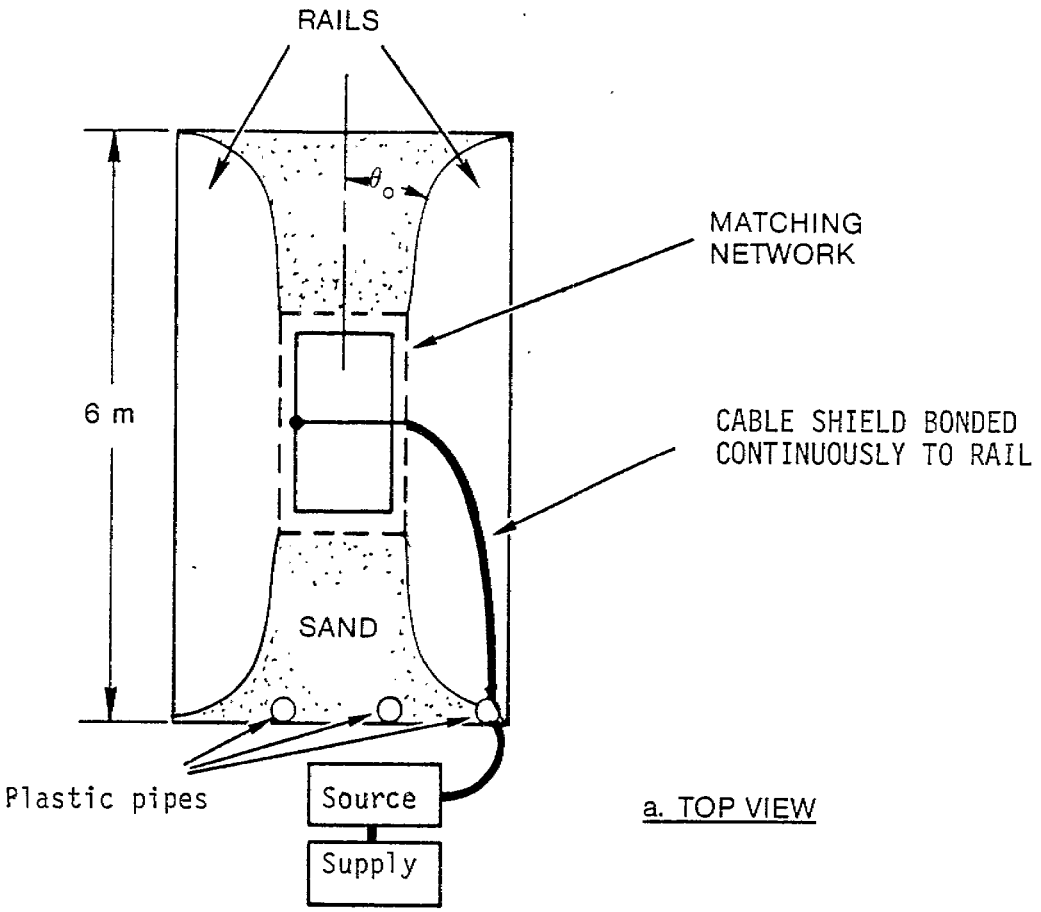

NOTE: DRAWINGS NOT TO SCALE

Figure 4. 2:1 (width 6 m; length 3 m) Inverse scale model test geometry.

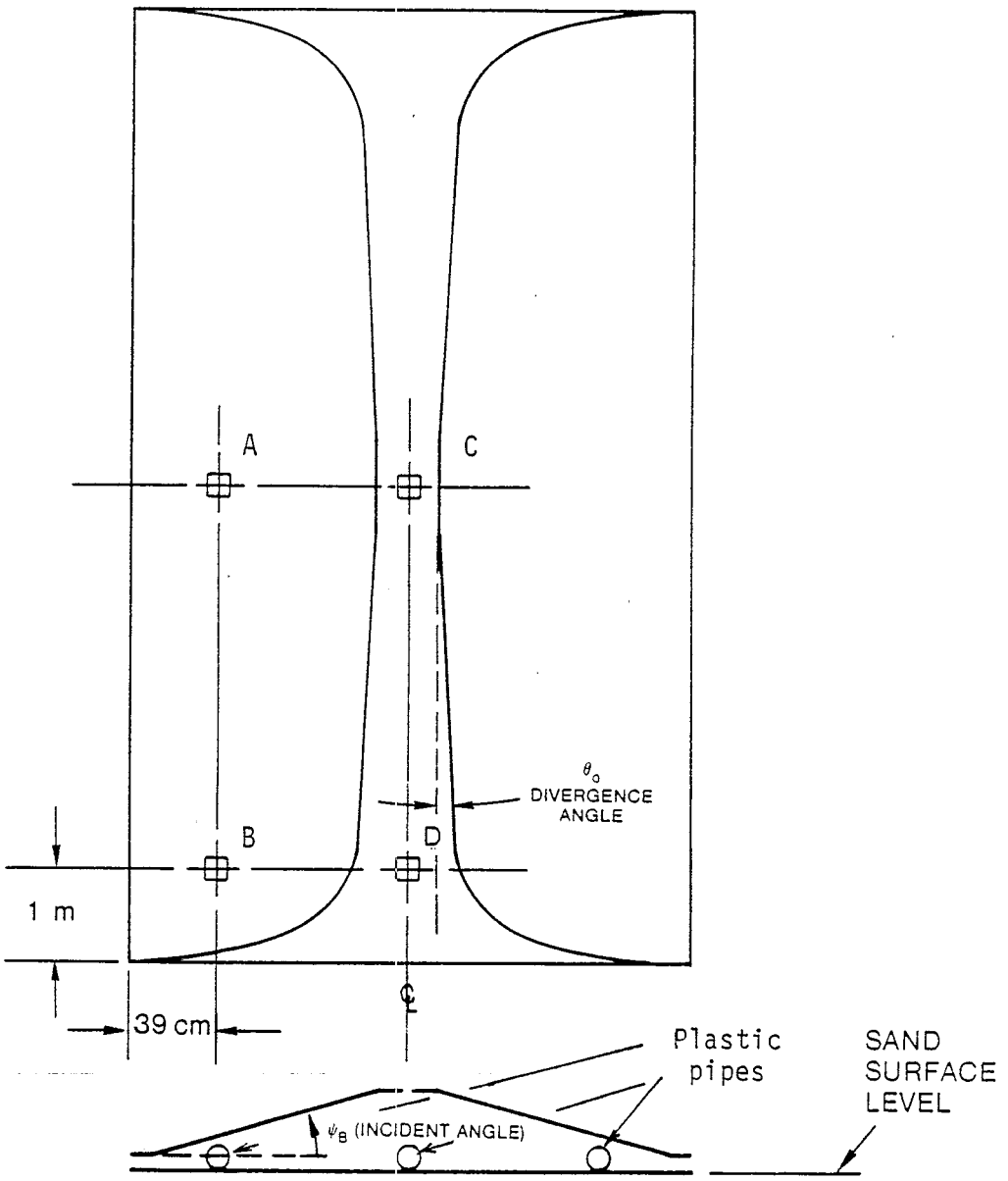

NOTE: DRAWINGS NOT TO SCALE

Figure 5. B-dot probe locations for the 2:1 inverse scale model tests.

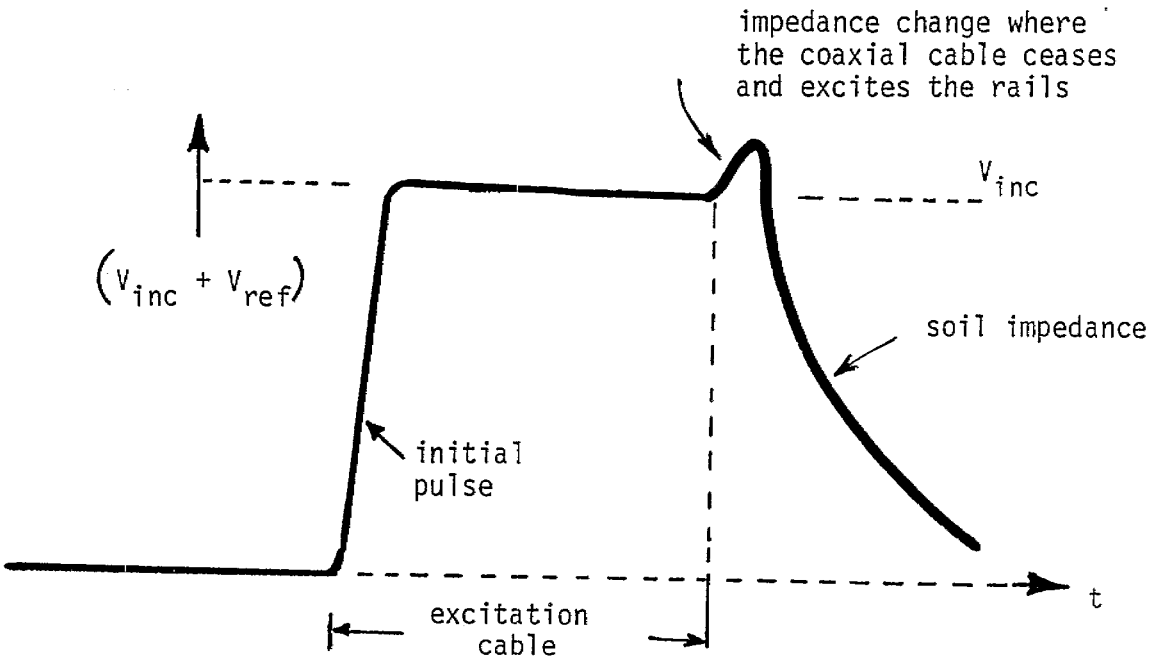

Figure 6. Typical TDR measurement.

NOTE: t is the elapsed time, from the start of the pulse divided by 2.

a) started with flat wings with θ_0 = 1.6° and elevated at a ψ_B = Brewster angle of 17°,
b) varied the elevation angle ψ_B (higher and lower),
c) lowered the spacing across the rail gap to 4 mm in order to lower the inductance mismatch at the feed point,
d) added a 15 cm high flange, which introduces capacitance for improved matching, and the gap increased to 5 cm to hold off 100 KV,
e) the corners of the rails were cut to a radius of curvature of 1.14 m,
f) the rail corners were bent towards the sand.

Some of the above experimental variations are illustrated in figure 7. Figure 8 shows representative TDR measurements. Figure 8a is the TDR data for the starting condition (a) above. When the elevation angle ψ_B was varied around the 17° value over the maximum achievable range, the variation in the TDR waveform was slight and the 17° value was chosen to be the optimum. When the gap spacing was lowered, it did lower the inductance mismatch, but did not completely eliminate it. The 15 cm high flanges were introduced, where the gap could be controlled for high voltage hold off (ex: gap = 5 cm for 100 KV pulse amplitude). The flanges introduce additional capacitance at the feed, which aids the impedance matching, as can be seen in figure 8b. The next step in optimization consisted of cutting the corners of the rails with a radius of curvature of 1·14 m and bending them toward the sand medium. The optimized TDR measurement is seen in figure 8c and the configuration of the optimized rails is sketched in figure 7.

Next, we turn our attention to the measured fields. Measurement of the magnetic field is relatively easier in free space or a material medium, such as sand in the present case, compared to the electric field. Although, it is possible to measure the electric field [10], for the present purposes of investigating the amplitude and rise time or the early time history of the fields, magnetic field measurement is adequate. The following pulse sources available and used in exciting the unit cell.

a) TEK109; 50 V, 250 ps; software integration of $\dot{B}(t)$
b) Maxwell 40151; 50 KV, $\leq$ 10 ns; direct drive, passive integration of $\dot{B}(t)$

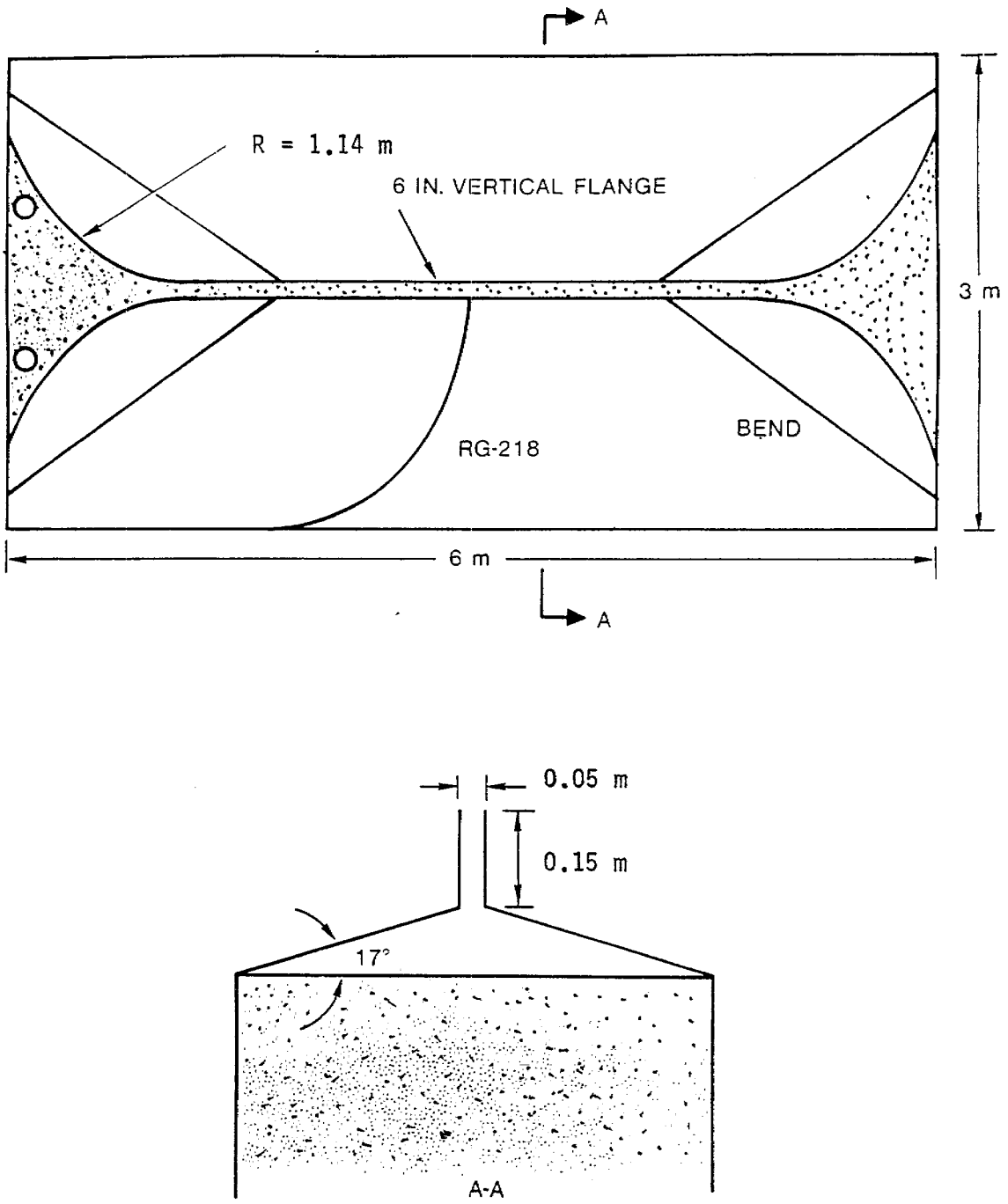

Figure 7. Illustration of some of the experimental variations.

a) Initial configuration
flat wings
$\theta_0 = 1.6°$
$\psi_B = 17°$

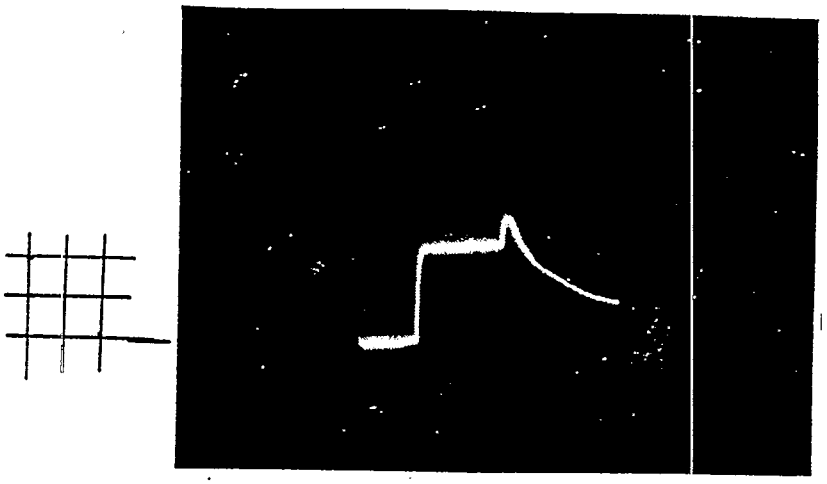

b) Intermediate configuration
vertical 0.15 m flanges, 0.05m gap
$\theta_0 = 1.6°$
$\psi_B = 17°$

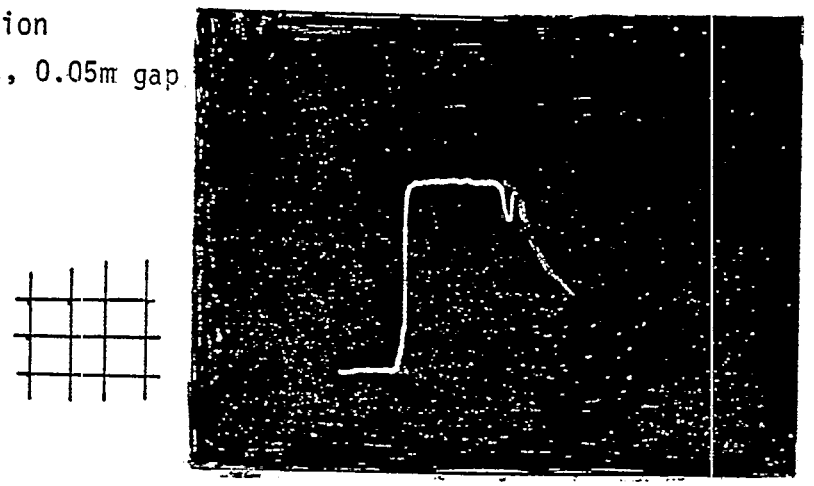

c) Final configuration
same as b with the rail
corners cut (R = 1.14 m)
and rails bent toward
the sand medium
R ≡ radius of curvature

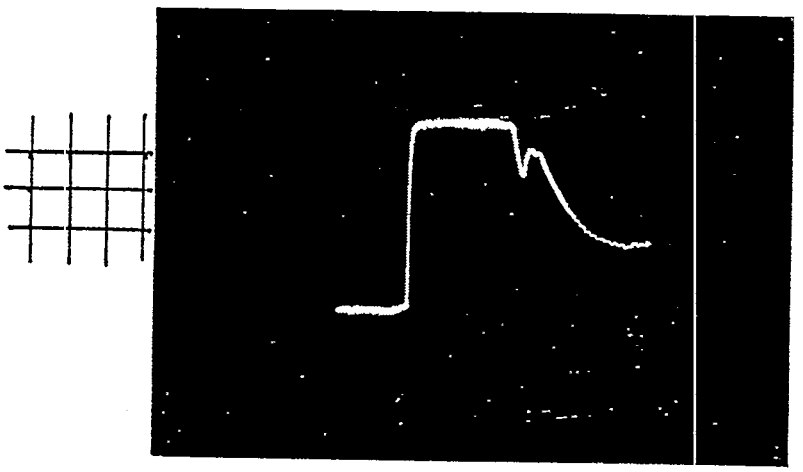

Figure 8. Rail shape optimization via TDR measurement.
NOTE: The vertical scale is $(V_{inc} + V_{ref})$ with V_{inc} corresponding to the flat top.

The horizontal scale is 20 ns/div., shown to the left of the scope trace.

c) Maxwell 40151; 50 KV, $\leq$ 10 ns; matching network to simulate a 2Ω driving point impedance, passive integration of $\dot{B}(t)$

d) Trigger generator; 100 KV, < 10 ns; passive integration of $\dot{B}(t)$

In the case of the TEK-109 source above, the measured $\dot{B}(t)$ is digitized and software integrated. In the remainder of the sources, passive integrators (1 μs) were used. The difference between cases b) and c) above is the use of a matching network in c). The matching network consisted of a 23Ω resistance in series with the two parallel 50Ω cables connecting the rails and a 2Ω resistor across the rails. This simulates a driving point impedance of 2Ω. The 100 KV source of case d) above was suspended above the rails using external wooden supports and connected to the rails with copper sheet extensions to the electrode attachments. The measured $\dot{B}(t)$ and derived $B(t)$ for the sources a) to d) above are shown in figures 10 to 13 and, the measurement locations are seen in figure 9.

Rather than analyze the data for the 2:1 model at this time, we report the results of 1:1 model of unit cell and also the results for a 3 × 3 array (Section 4) and defer the analysis of the experimental data to Section 5.

B. 1:1 (width to length ratio) model

The 1:1 model, similar to the 2:1 model is shown in figure 13. The difference between the two being that w ≡ width = 3m as opposed to 6m in the previous case. The 1:1 rails were originally patterned after the optimized 2:1 model with a 5 cm gap spacing and the 15 cm flanges. The TDR waveform immediately showed this to be an inappropriate shape for the 1:1 model. The rails were modified while monitoring the TDR waveform. The bend in the rails were straightened and the vertical flanges removed. Next, the divergence angle was slowly increased, ending with a divergence half angle θ_0 = 12°. The initial TDR, the final TDR and the final (optimized) 1:1 rail shape are shown in figure 15.

As before, the four sources i.e., TEK 109, Maxwell 40151 with and without matching network, and a 100 KV pulse source were used and the B-dot data recorded at 4 locations on the sand surface. The results are shown in figures 16 to 20.

In concluding this section, we note that representative TDR and magnetic field data is presented here for two configurations (rectangular 2:1 and a square) of a unit cell, with four different source configurations.

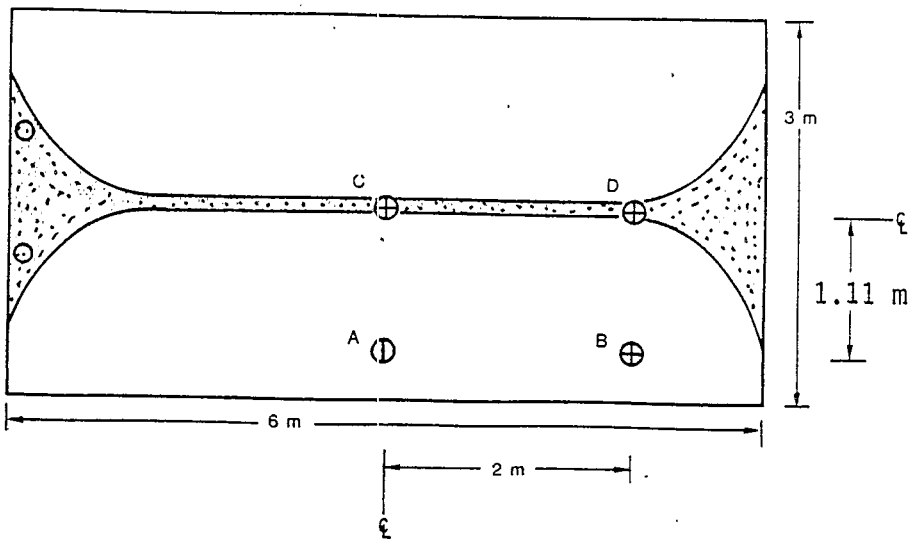

Figure 9. Four locations (A,B,C,D) where the field measurements were made

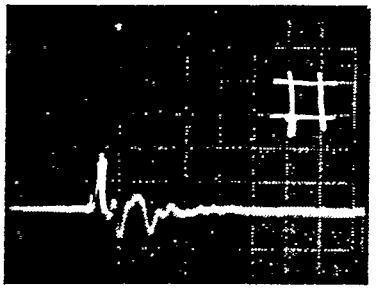

(a) POSITION A
5 ns/DIV 5 T/s/DIV

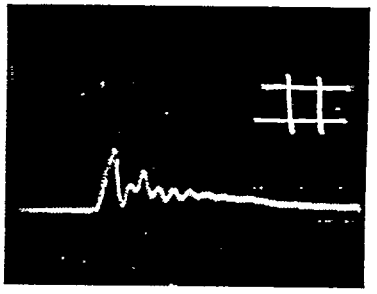

(c) POSITION C
5 ns/DIV 10 T/s/DIV

$\dot{B}(t)$

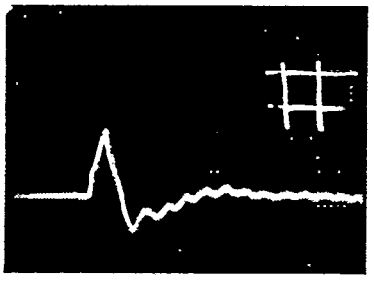

(b) POSITION B
5 ns/DIV 2.5 T/s/DIV

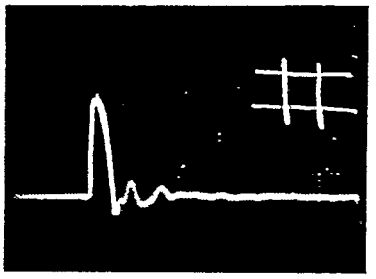

(d) POSITION D
5 ns/DIV 10 T/s/DIV

Figure 10. $\dot{B}(t)$ measurements with TEK-109 as the source (50 v, 250 ps).

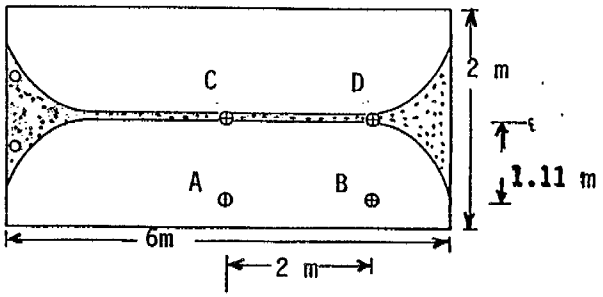

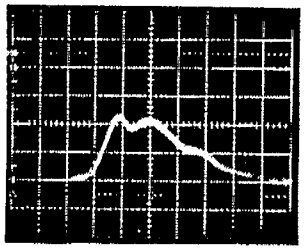

(a) POSITION A
5 ns/DIV 5000 T/s/DIV

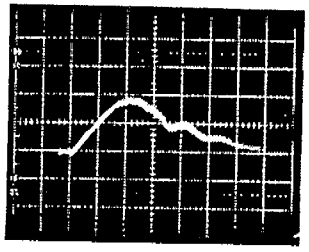

(c) POSITION C
5 ns/DIV 5000 T/s/DIV

$\dot{B}(t)$

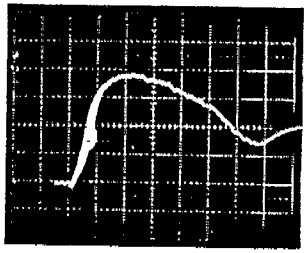

(a) POSITION A
20 ns/DIV 50 μT/DIV

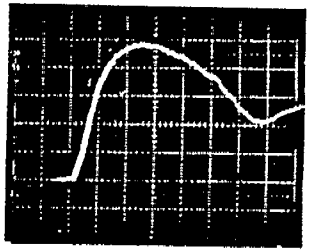

(c) POSITION C
20 ns/DIV 50 μT/DIV

B(t)

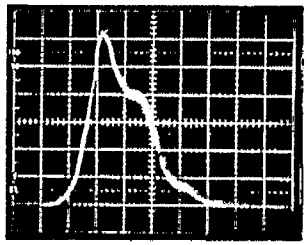

(b) POSITION B
5 ns/DIV 2500 T/s/DIV

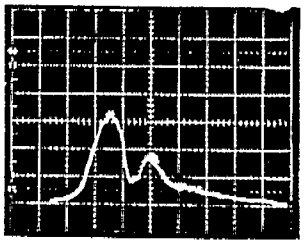

(d) POSITION D
5 ns/DIV 5000 T/s/DIV

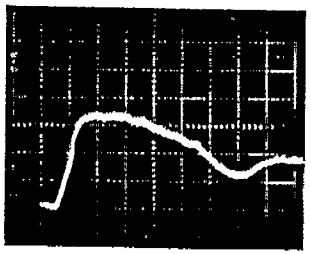

(b) POSITION B
20 ns/DIV 50 μT/DIV

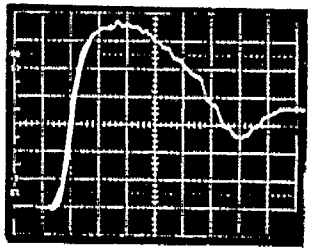

(d) POSITION D
20 ns/DIV 25 μT/DIV

Figure 11. $\dot{B}(t)$ and B(t) data with Maxwell 40151 (50 KV, $\leq$ 10 ns, direct drive) source.

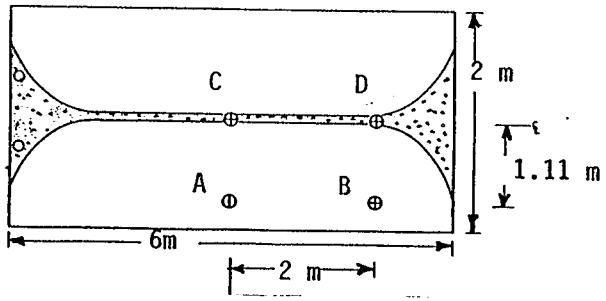

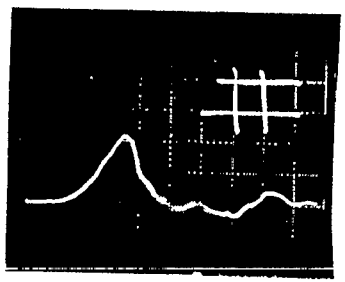

(a) POSITION A
5 ns/DIV 500 T/s/DIV

$\dot{B}(t)$

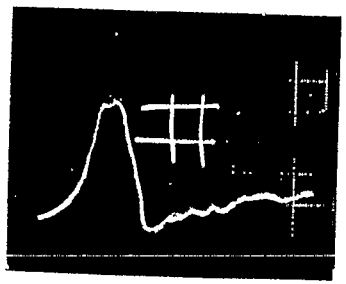

(c) POSITION C
5 ns/DIV 500 T/s/DIV

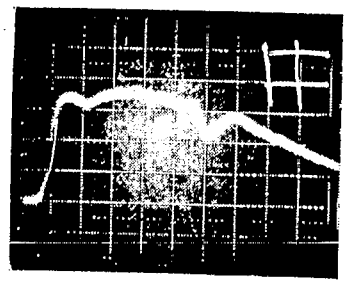

(a) POSITION A
20 ns/DIV 5 μT/DIV

$B(t)$

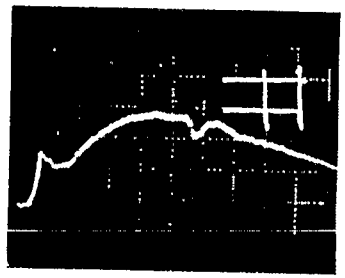

(c) POSITION C
20 ns/DIV 5 μT/DIV

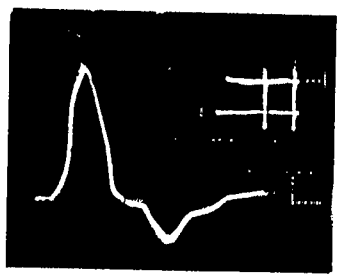

(b) POSITION B
5 ns/DIV 1000 T/s/DIV

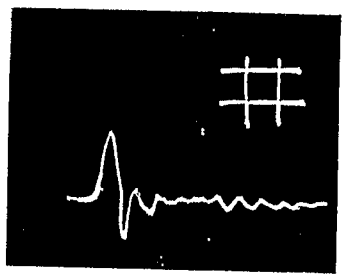

(d) POSITION D
10 ns/DIV 2500 T/s/DIV

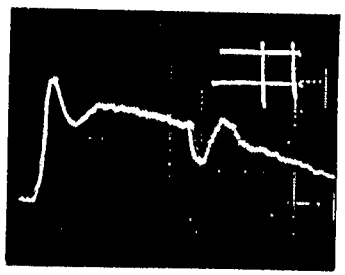

(b) POSITION B
20 ns/DIV 5 μT/DIV

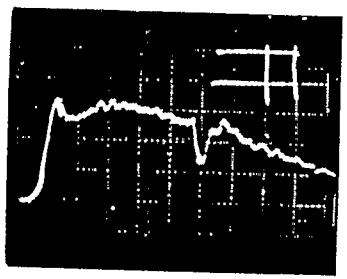

(d) POSITION D
20 ns/DIV 5 μT/DIV

Figure 12. $\dot{B}(t)$ and $B(t)$ data with Maxwell 40151 (50 KV, < 10 ns, matching network) source.

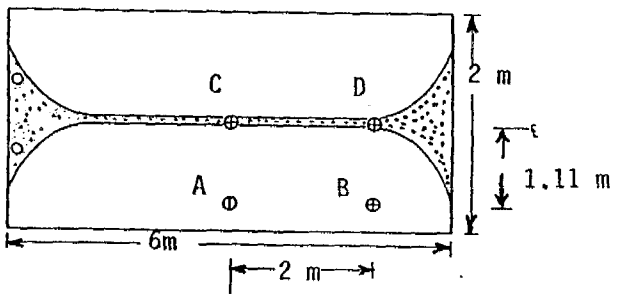

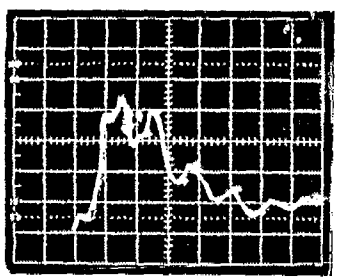

(a) POSITION A
5 ns/DIV 5000 T/s/DIV

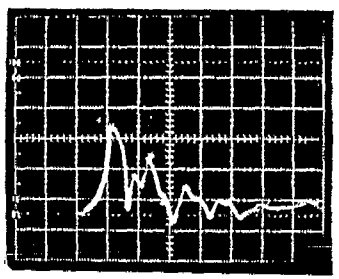

(c) POSITION C
5 ns/DIV 10,000 T/s/DIV

$\dot{B}(t)$

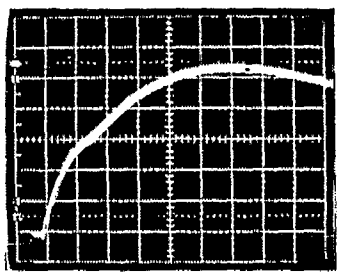

(a) POSITION A
20 ns/DIV 100 μT/DIV

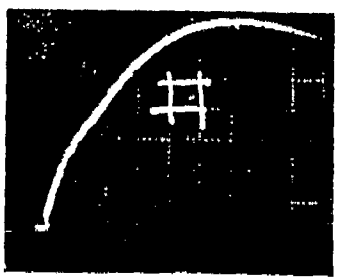

(c) POSITION C
20 ns/DIV 100 μT/DIV

B(t)

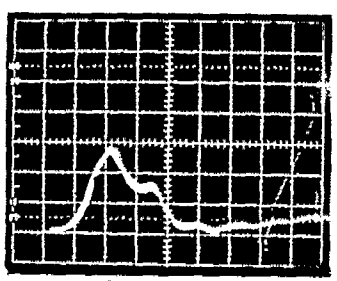

(b) POSITION B
5 ns/DIV 10,000 T/s/DIV

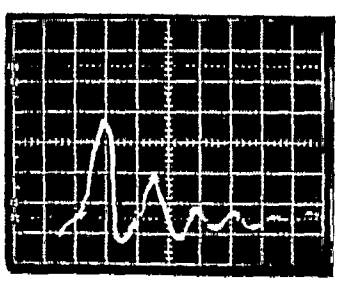

(d) POSITION D
5 ns/DIV 10,000 T/s/DIV

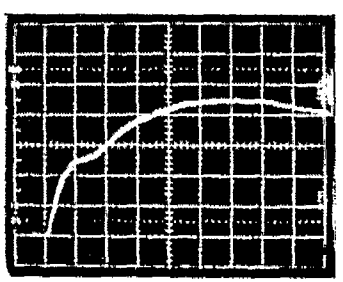

(b) POSITION B
20 ns/DIV 100 μT/DIV

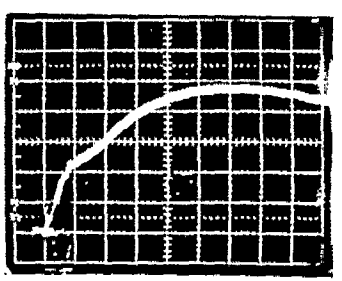

(d) POSITION D
20 ns/DIV 100 μT/DIV

Figure 13. B(t) and B(t) dat[illegible]th a 100 KV, < 10 ns pulse source.

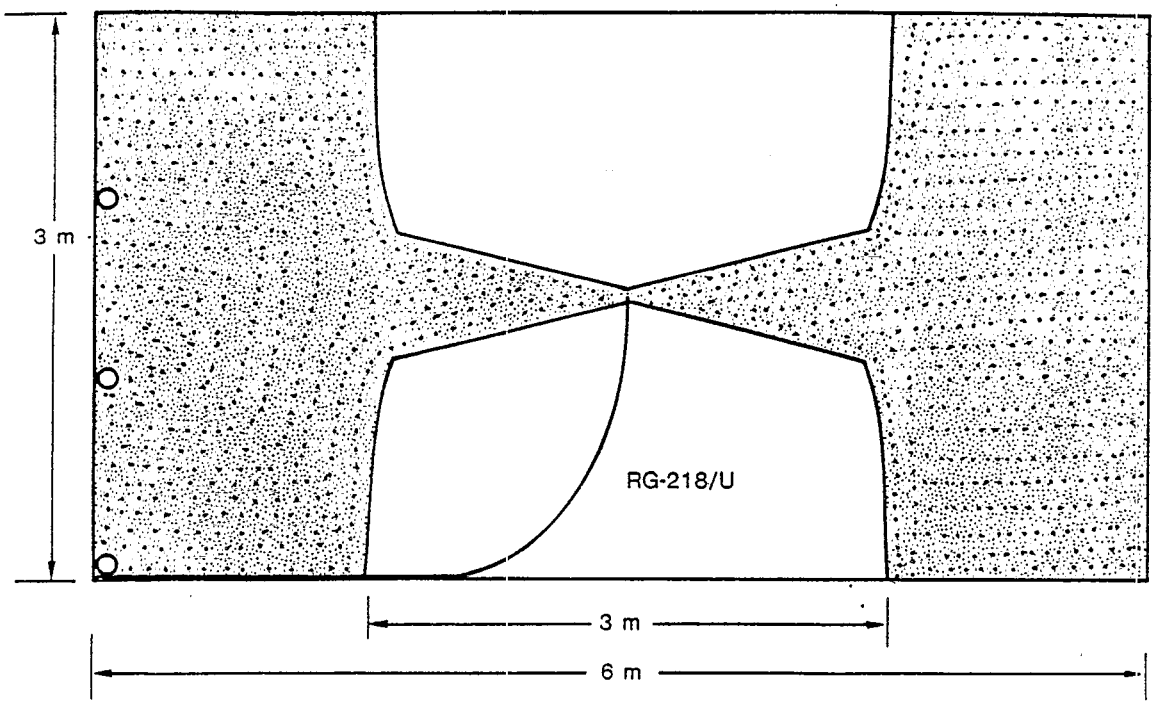

Figure 14. 1:1 (width to length ratio) Model of a unit cell.

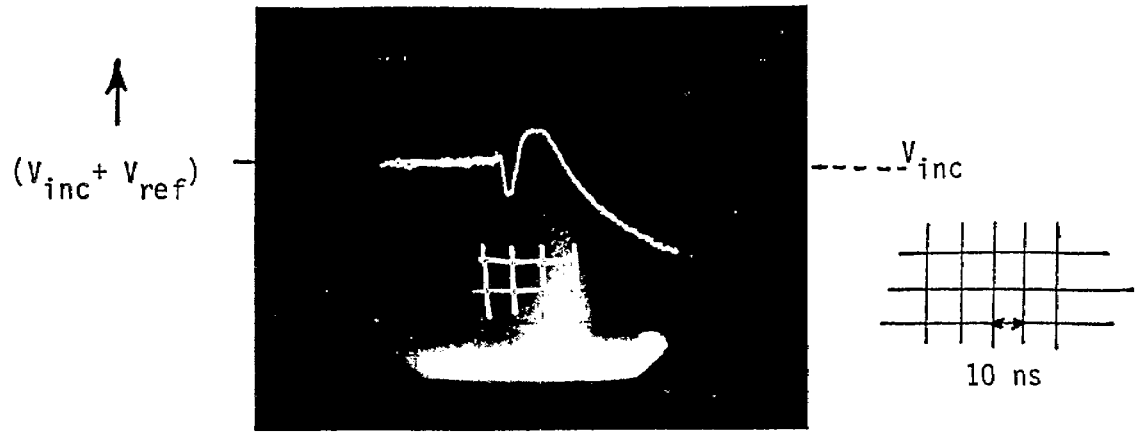

(a) ORIGINAL RAILS

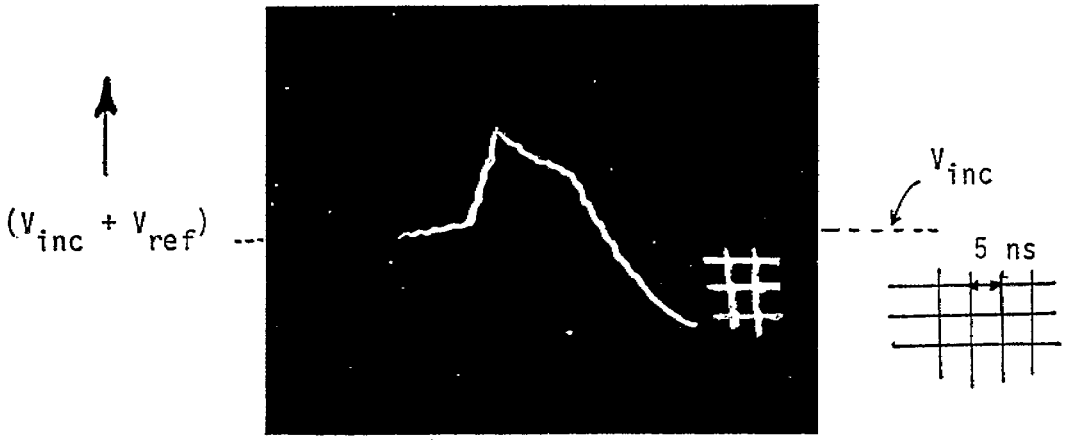

(b) OPTIMIZED RAILS

a) Initial and final (i.e., optimized) TDR measurement

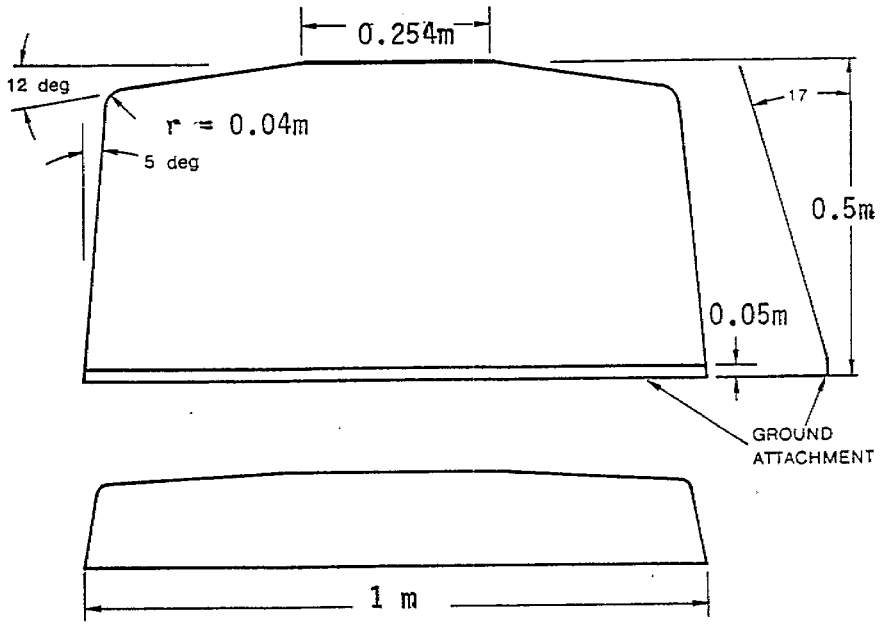

b) Optimized 1:1 model configuration

Figure 14. 1:1 rail optimization via TDR measurement.

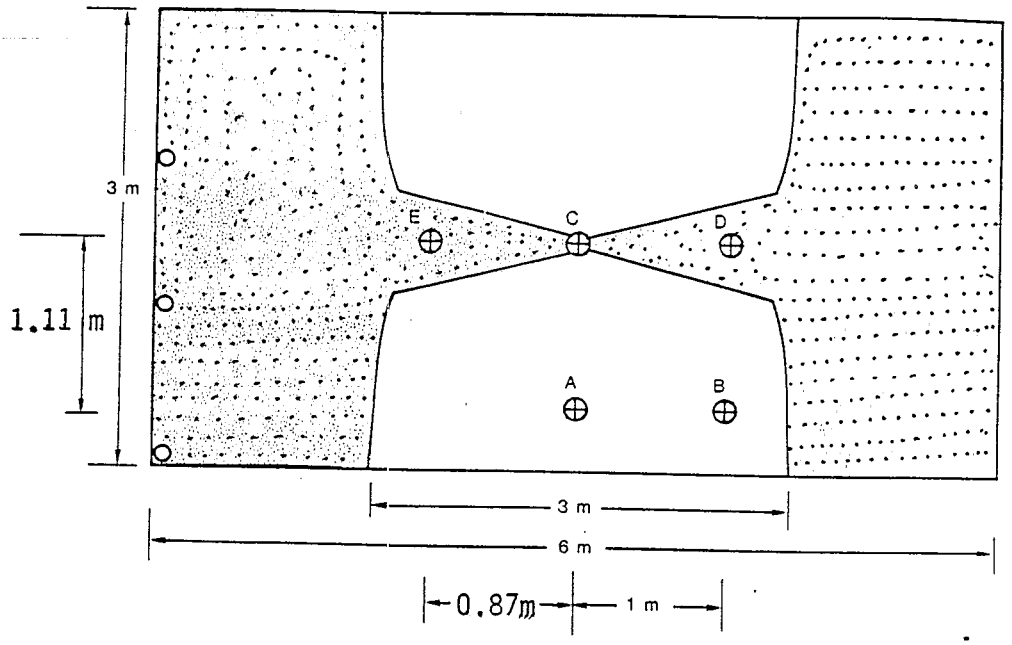

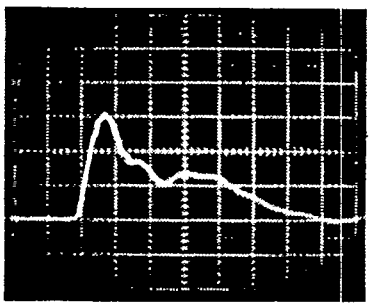

(a) POSITION A
2 ns/DIV 10 T/s/DIV

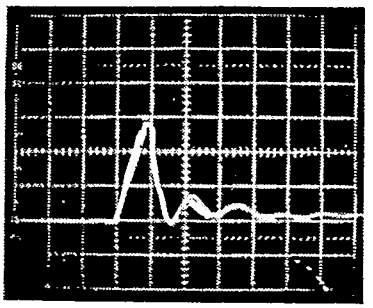

(c) POSITION C
2 ns/DIV . 25 T/s/DIV

$\dot{B}(t)$

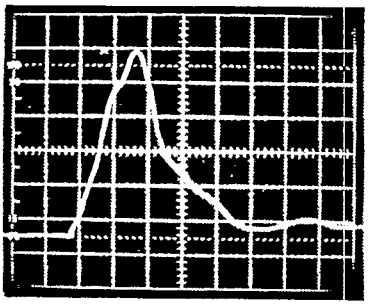

(b) POSITION B
2 ns/DIV 5 T/s/DIV

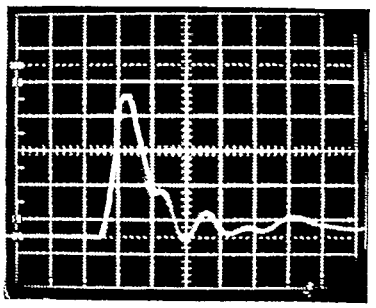

(d) POSITION D
2 ns/DIV 10 T/s/DIV

Figure 16. $\dot{B}(t)$ measurements with TEK-109 as the source (50 V, 250 ps).

NOTE: Positions A, B, C, D, are on sand surface while position E is 31 cm below the interface.

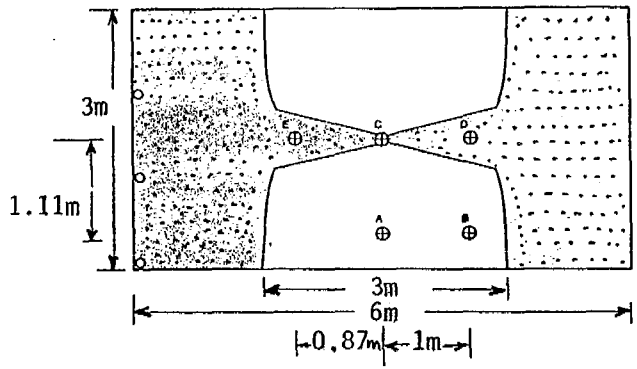

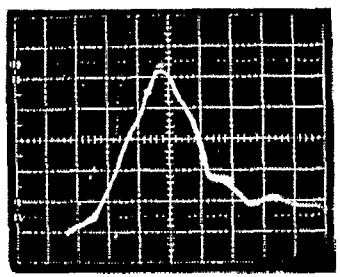

(a) POSITION A
5 ns/DIV 2500 T/s/DIV

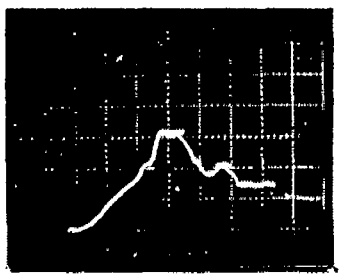

(c) POSITION C
5 ns/DIV 4000 T/s/DIV

$\dot{B}(t)$

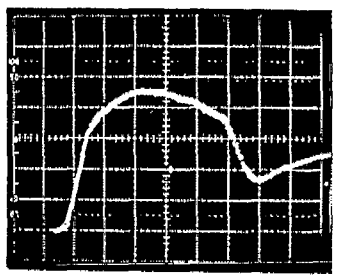

(a) POSITION A
20 ns/DIV 50 μT/DIV

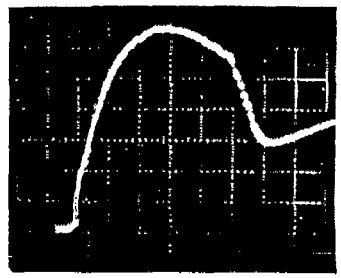

(c) POSITION C
20 ns/DIV 50 μT/DIV

B(t)

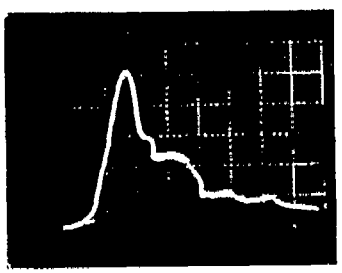

(b) POSITION B
5 ns/DIV 4000 T/s/DIV

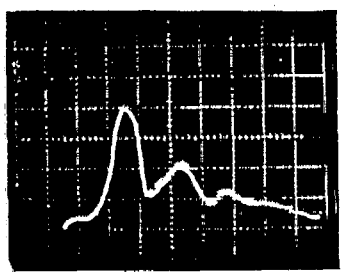

(d) POSITION D
5 ns/DIV 4000 T/s/DIV

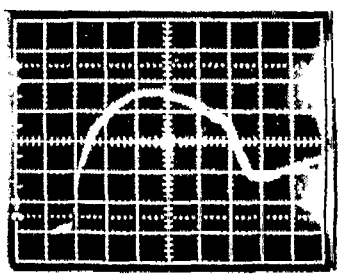

(b) POSITION B
20 ns/DIV 50 μT/DIV

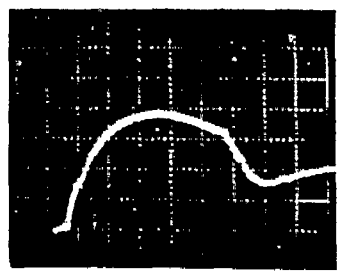

(d) POSITION D
20 ns/DIV 50 μT/DIV

Figure 17. $\dot{B}(t)$ and B(t) data with Maxwell 40151 (50 KV, $\leq$ 10 ns, direct drive source).

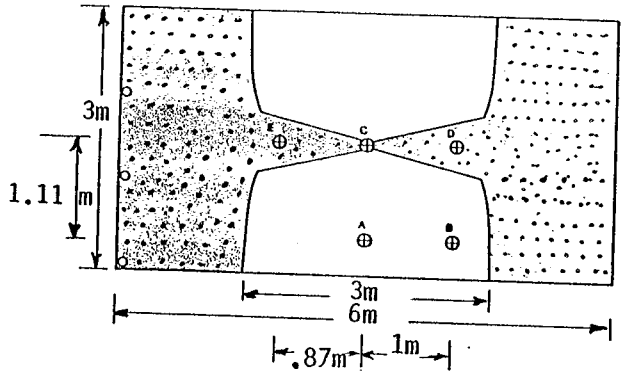

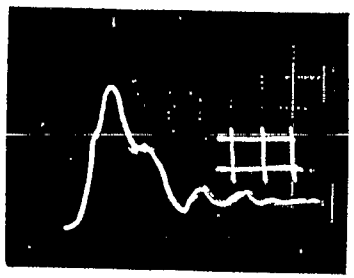

(a) POSITION A
5 ns/DIV 250 T/s/DIV

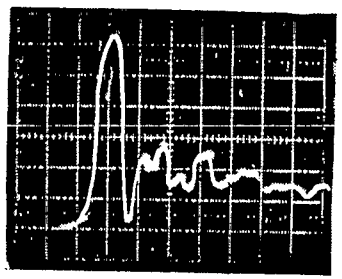

(c) POSITION C
5 ns/DIV 250 T/s/DIV

$\dot{B}(t)$

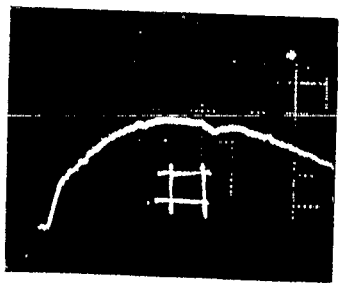

(a) POSITION A
20 ns/DIV 5 μT/DIV

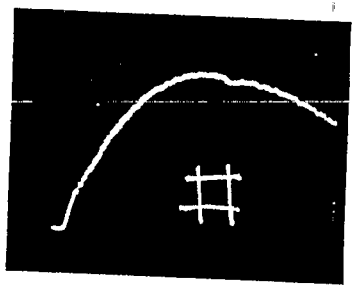

(c) POSITION C
20 ns/DIV 5 μT/DIV

B(t)

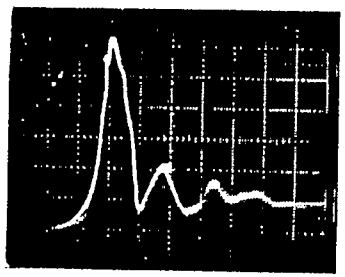

(b) POSITION B
5 ns/DIV 250 T/s/DIV

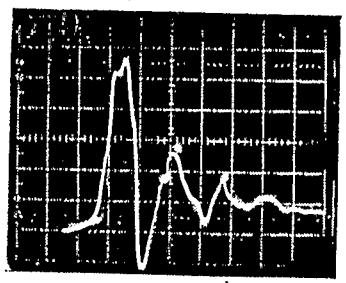

(d) POSITION D
5 ns/DIV 250 T/s/DIV

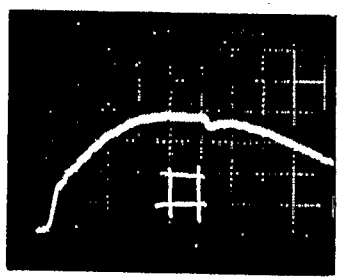

(b) POSITION B
20 ns/DIV 5 μT/DIV

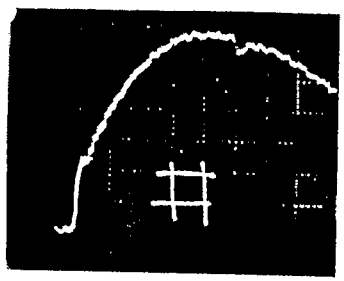

(d) POSITION D
20 ns/DIV 2.5 μT/DIV

Figure 18. $\dot{B}(t)$ and B(t) data with Maxwell 40151 (50 KV, < 10 ns, matching network) source.

B_{pk} = 16.3 μT

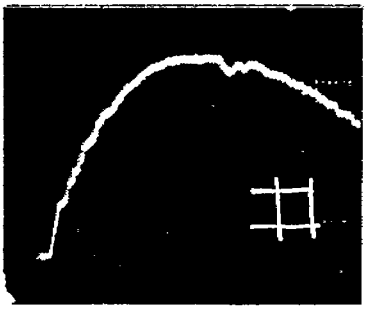

DEPTH = 0 m

20 ns/DIV 2.5 μT/DIV

(a) POSITION D

B_{pk} = 14.3 μT

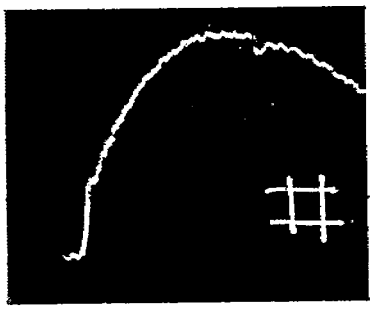

DEPTH = 0.31 m

20 ns/DIV 2.5 μT/DIV

(b) POSITION E

Figure 19. B(t) at the sand surface (Position D) and at a depth of 31 cm (Position E) with a Maxwell 40151 (50 KV, < 10 ns, matching network) source.

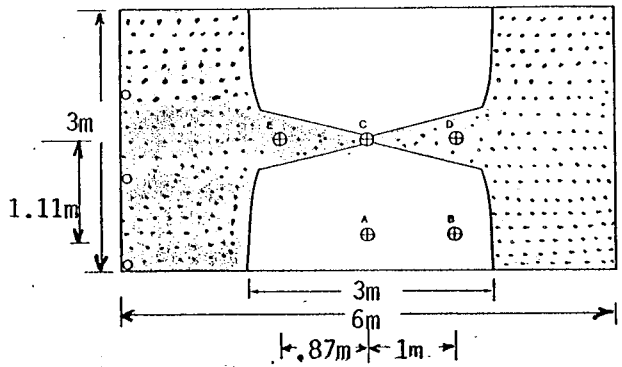

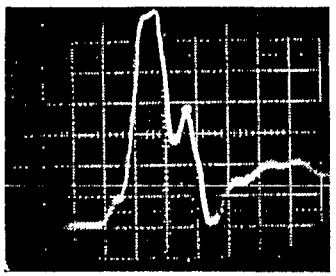

(a) POSITION A
5 ns/DIV 4000 T/s/DIV

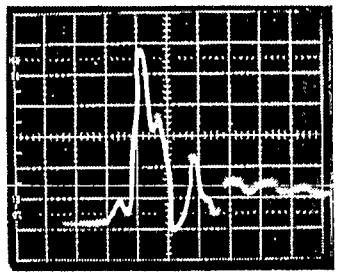

(c) POSITION C
5 ns/DIV 10,000 T/s/DIV

$\dot{B}(t)$

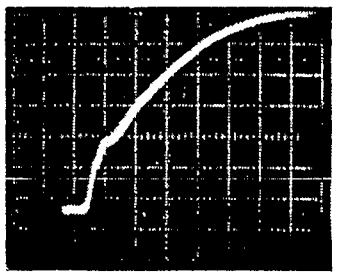

(a) POSITION A
20 ns/DIV 100 μT/DIV

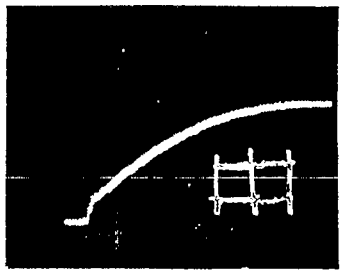

(c) POSITION C
20 ns/DIV 250 μT/DIV

$B(t)$

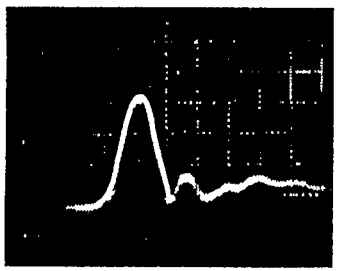

(b) POSITION B
5 ns/DIV 10,000 T/s/DIV

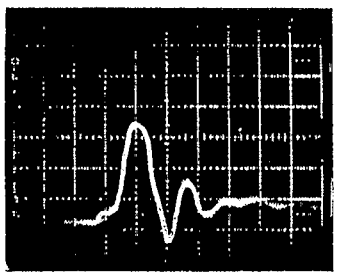

(d) POSITION D
5 ns/DIV 10,000 T/s/DIV

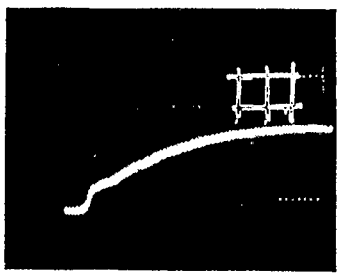

(b) POSITION B
20 ns/DIV 250 μT/DIV

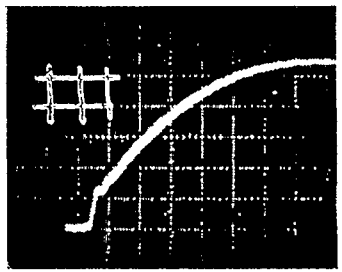

(d) POSITION D
20 ns/DIV 100 μT/DIV

Figure 20. $\dot{B}(t)$ and $B(t)$ data with a 100 KV, < 10 ns pulse source.

In the following Section 4, we turn our attention to a 3×3 (or 9 pulser) array of pulsers before proceeding to analyze the experimental results.

4. Experimental Results on a 3 × 3 Pulser Array

The 3 3 array of 9 pulse sources were employed to drive fields into the same sandbox as in figure 2 of size 6m 3m. Consequently, the area of a unit cell is (1/9)th of 18 sq.m. or 2 sq.m. The unit cell consists of 2:1 model rail configuration, patterned after the results in Section 3A. The array can be configured in an in-line fashion or a staggered fashion [1]. Also, the array can be excited simultaneously or in a swept fashion. These possibilities result in the following four experimental configurations

1. In-line array, simultaneous drive
2. In-line array, swept drive
3. Staggered array, simultaneous drive
4. Staggered array, swept drive

In addition, each of the above 4 pulser arrays has been driven by a TEK-109 (50 v, 250 ps) source and also the Maxwell 40151 (50 KV, < 10 ns) source. MGL-6A B-dot probe, bonded RG-402 cables and Tektronix 485 oscilloscope were used in measuring and recording the magnetic field data. From a single source, a nine-way fan out arrangement shown in figure 21 was employed to drive the 9 "switch gaps." The four experimental configurations listed above are schematically shown in figures 22 and 23. Also shown in these figures are positions where magnetic field data is recorded. The swept mode is accomplished by controlling the cable lengths from the fan out. This simulates a wave propagation in the +x direction in figures 22 and 23.

A. In-line simultaneous drive (figure 22a)

In this set of measurements, the 9 pulsers are driven simultaneously and the measured data ($\dot{B}$) recorded at positions A to F with the TEK-109 (50 v, 250 ps) and the Maxwell 40151 (50 KV, < 10 ns) sources. These measurements are shown in figures 24 and 25.

B. In-line swept drive (figure 22b)

In this set of measurements, the 9 pulsers are driven in a swept mode (i.e., 1 row at a time) and $\dot{B}(t)$ is recorded at positions A to I with the TEK-109 (50 v, 250 ps) and the Maxwell 40151 (50 KV, < 10 ns) sources. These measurements are shown in figures 26 and 27.

C. Staggered array with simultaneous drive (figure 23a)

In this set of measurements, the 9 pulsers are driven simultaneously

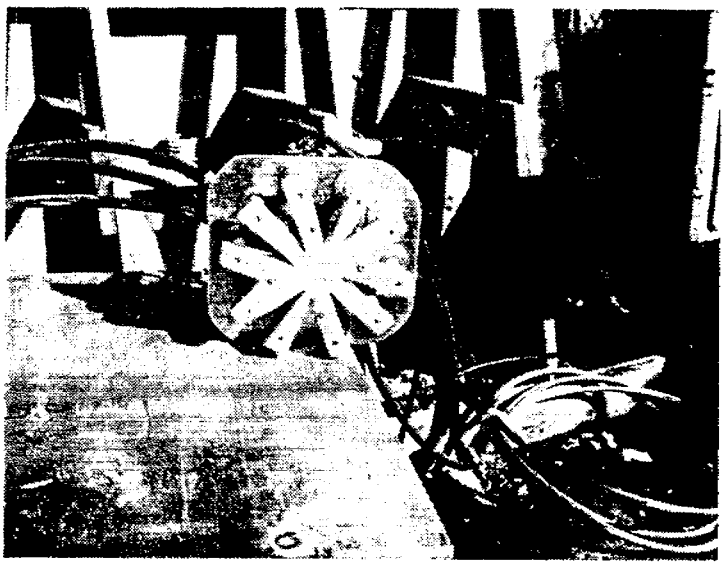

(a) VIEW OF FAN-OUT

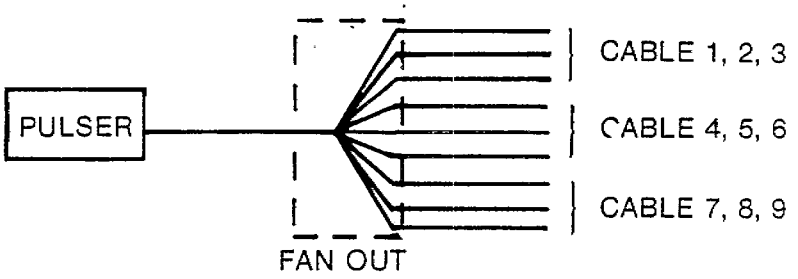

(b) DIAGRAM OF FAN-OUT

Figure 21. Nine way fan out arrangement to feed nine "switch gaps" from a single source.

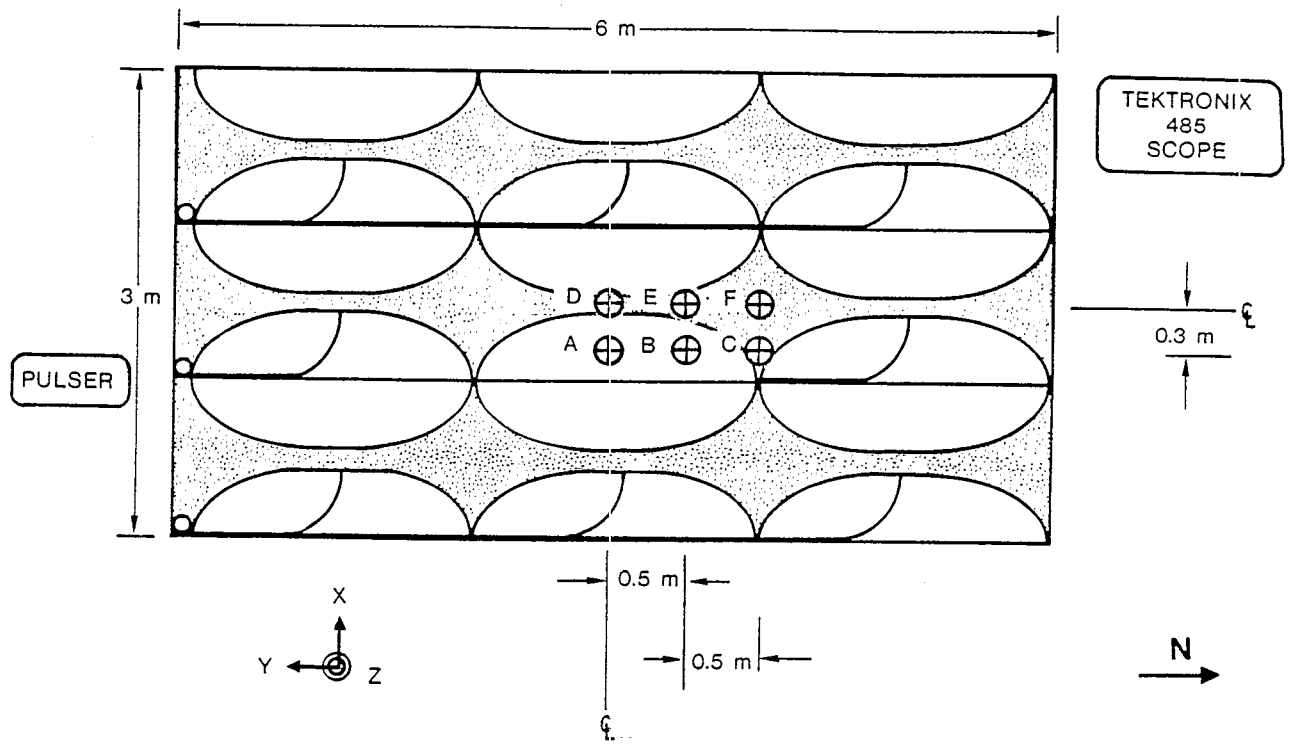

(a)

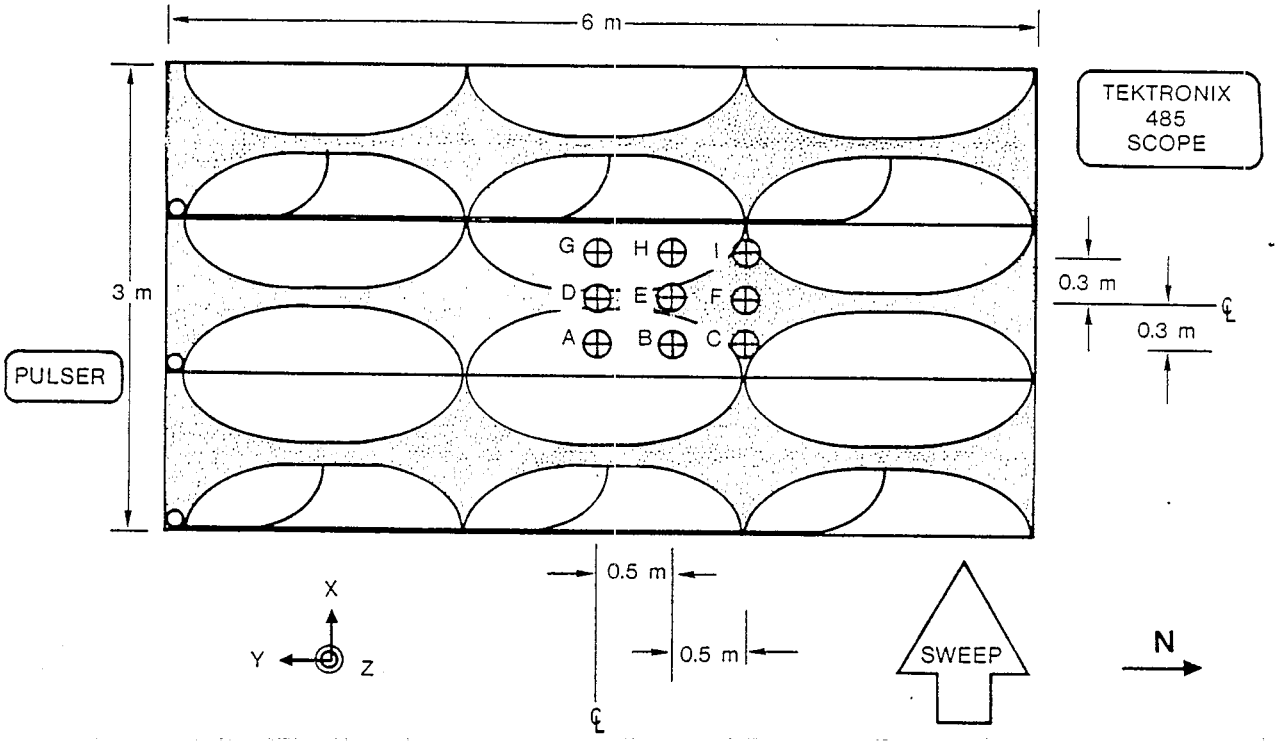

(b)

Figure 22. In-line 3 × 3 pulser array
a) simultaneous drive b) swept drive

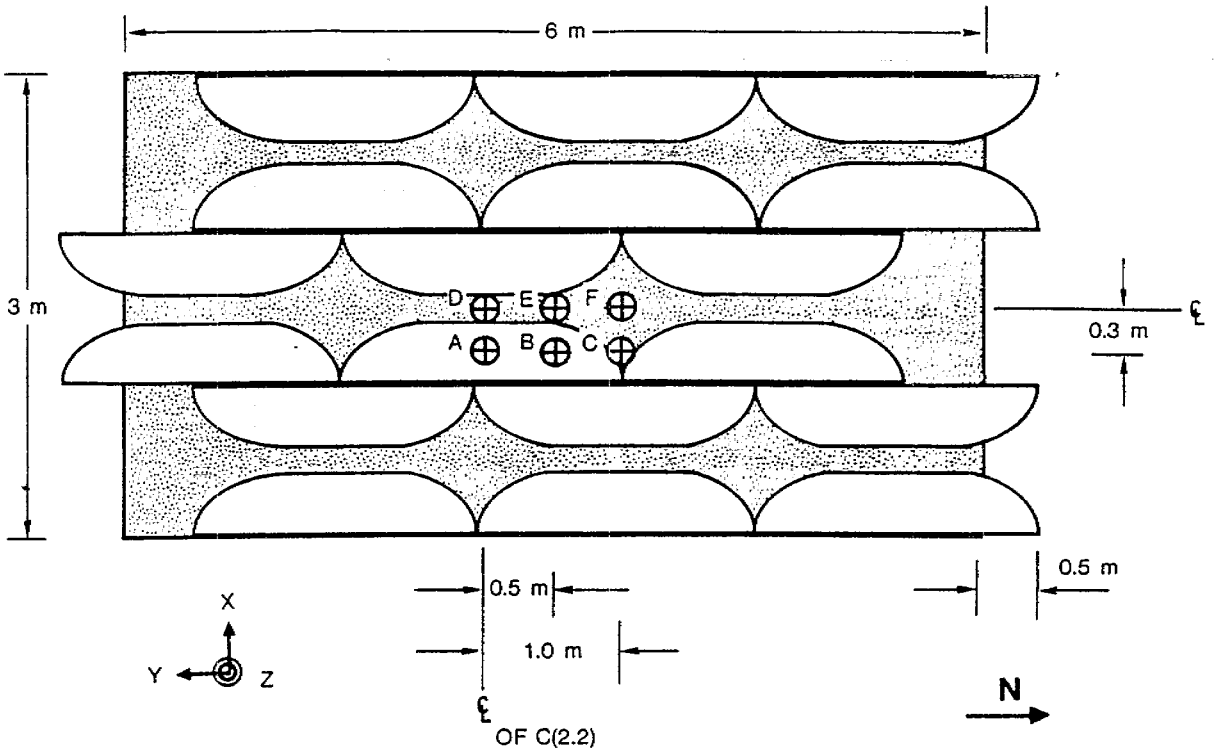

(a)

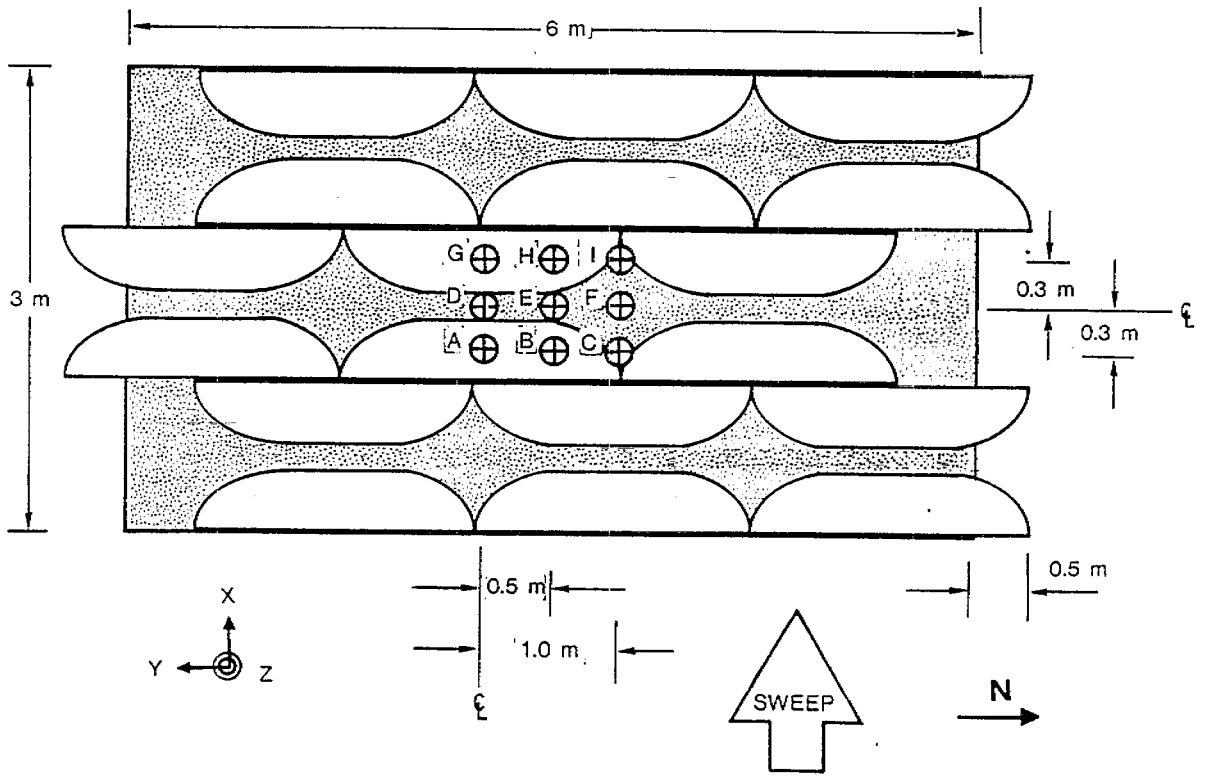

(b)

Figure 23. Staggered 3 × 3 pulser array
a) simultaneous drive b) swept drive

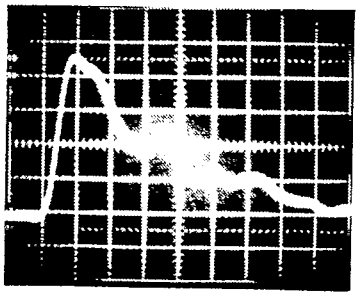

POSITION A
2.5 T/s/DIV

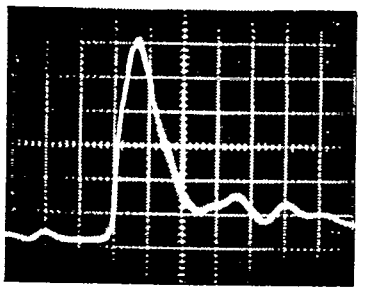

POSITION D
5 T/s/DIV

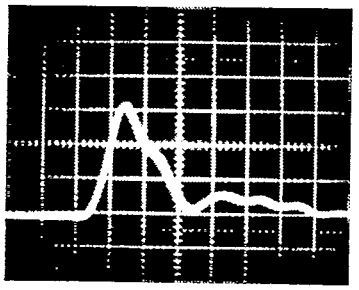

POSITION B
5 T/s/DIV

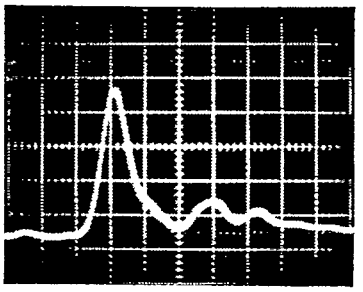

POSITION E
5 T/s/DIV

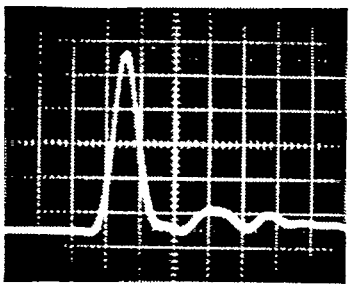

POSITION C
5 T/s/DIV

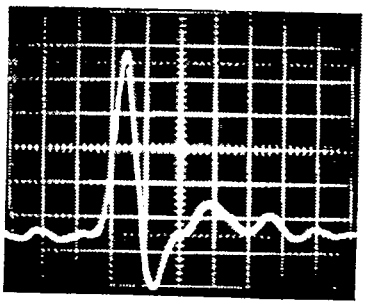

POSITION F
5 T/s/DIV

SWEEP SPEED; 2 ns/DIV

Figure 24. B(t) measured in an in-line, simultaneously driven array (3 × 3) with a TEK-109 (50 V, 250 ps) source.

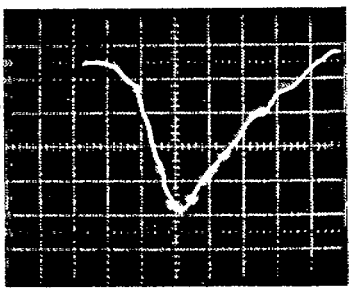

(a) POSITION A
5 ns/DIV 5000 T/s/DIV

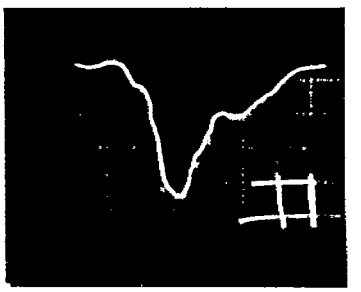

(d) POSITION D
5 ns/DIV 10,000 T/s/DIV

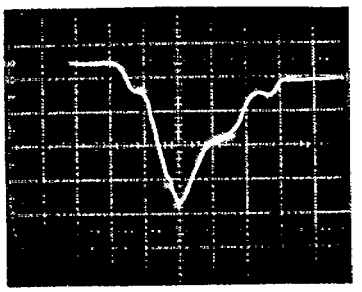

(b) POSITION B
5 ns/DIV 5000 T/s/DIV

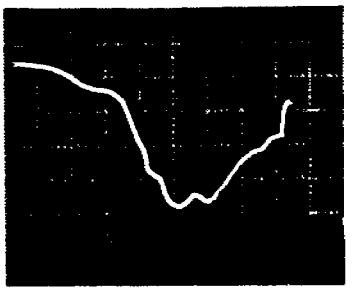

(e) POSITION E
2 ns/DIV 5000 T/s/DIV

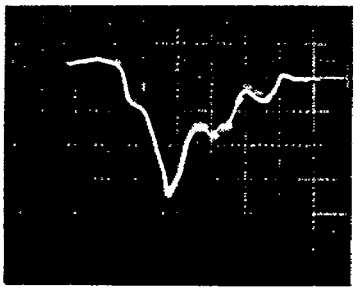

(c) POSITION C
5 ns/DIV 5000 T/s/DIV

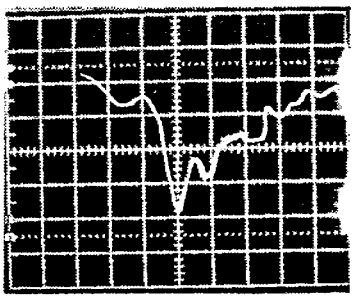

(f) POSITION F
2 ns/DIV 5000 T/s/DIV

Figure 25. $\dot{B}(t)$ measured in an in-line simultaneously driven array (3×3) with a Maxwell 40151 (50 KV, $\leq$ 10 ns) source.

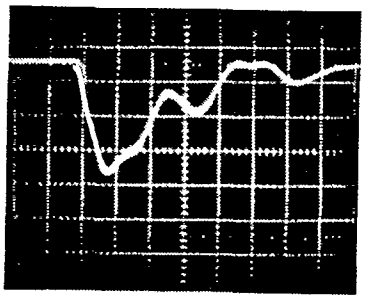

(a) POSITION A

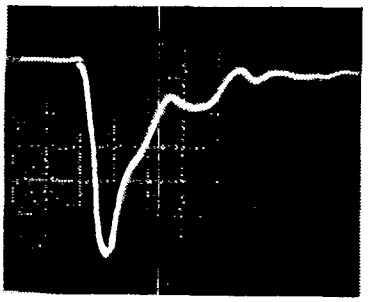

(d) POSITION D

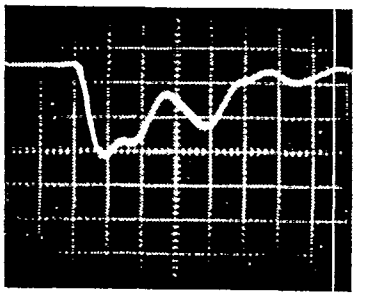

(g) POSITION G

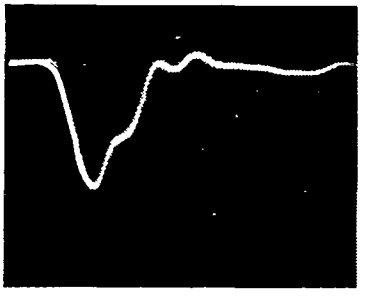

(b) POSITION B

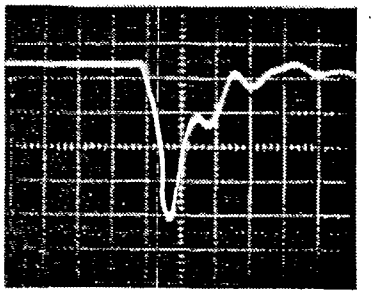

(e) POSITION E

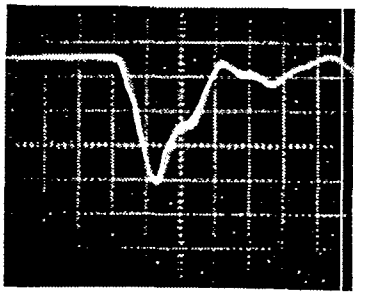

(h) POSITION H

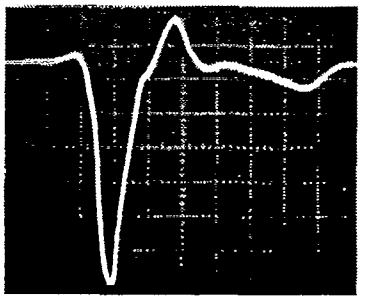

(c) POSITION C

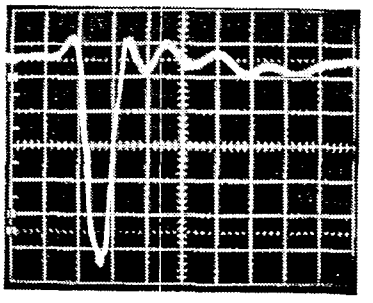

(f) POSITION F

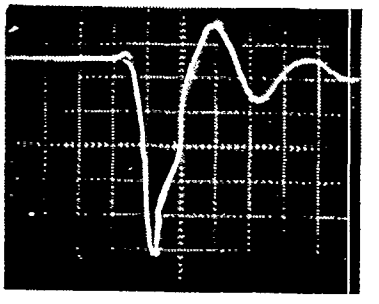

(i) POSITION I

SWEEP SPEED: 2 ns/DIV VERTICAL SCALE: 5 T/s/DIV

Figure 26. $\dot{B}(t)$ measured in an in-line, swept driven array (3×3) with a TEK 109 (50 V, 250 ps) source.

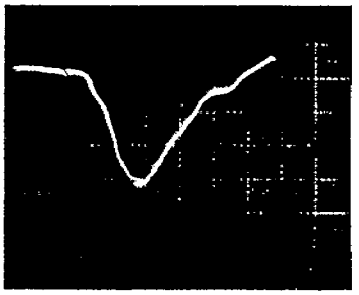

(a) POSITION A
5000 T/s/DIV

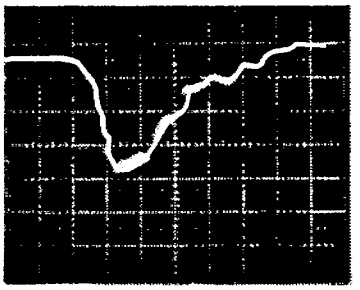

(d) POSITION D
10,000 T/s/DIV

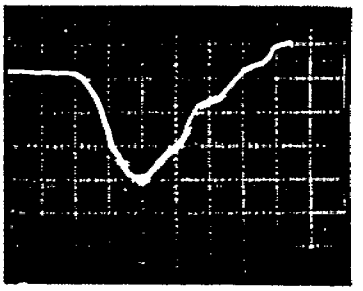

(g) POSITION G
5000 T/s/DIV

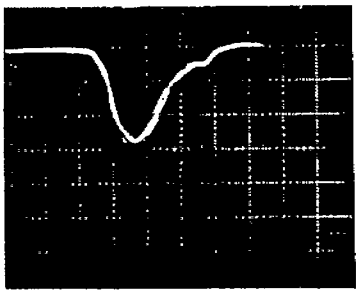

(b) POSITION B
5000 T/s/DIV

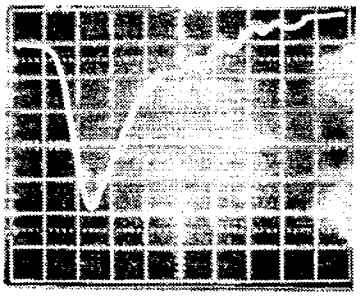

(e) POSITION E
5000 T/s/DIV

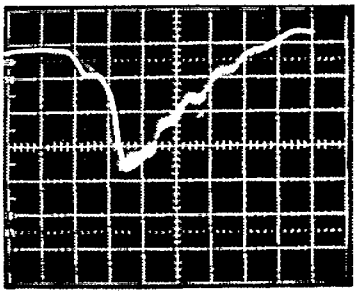

(h) POSITION H
5000 T/s/DIV

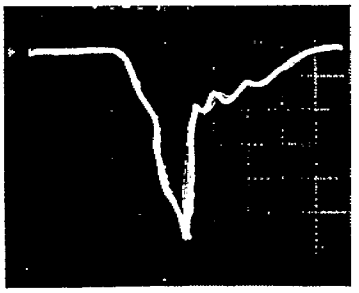

(c) POSITION C
5000 T/s/DIV

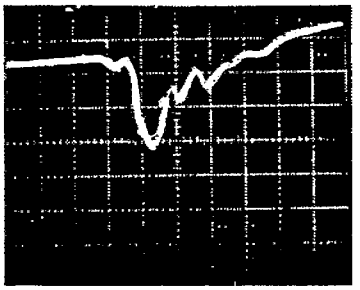

(f) POSITION F
5000 T/s/DIV

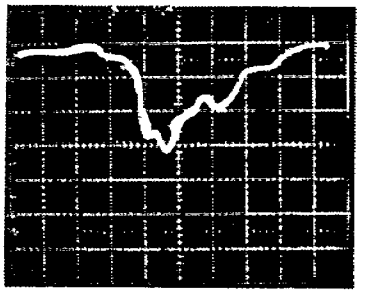

(i) POSITION I
5000 T/s/DIV

SWEEP SPEED: 5ns/DIV

Figure 27. $\dot{B}(t)$ measured in an in-line swept array (3 × 3) with a Maxwell 40151 (50 KV, < 10 ns) source.

and the measured data ($\dot{B}$) recorded at positions A to F with the TEK-109 (50 v, 250 ps) and the Maxwell 40151 (50 KV, < 10 ns) sources. These measurements are shown in figures 28 and 29.

D. Staggered array with swept drive (figure 22b)

In this set of measurements, the 9 pulsers are driven in a swept mode (i.e., one row at a time) and $\dot{B}(t)$ is recorded at positions A to I with the TEK-109 (50 v, 250 ps) and the Maxwell 40151 (50 KV, < 10 ns) sources. These measurements are shown in figures 30 and 31.

We conclude this section by noting that the measured $\dot{B}(t)$ and in some cases derived $B(t)$ have been reported for a rectangular (2:1) rail model, a square model and a 3 × 3 pulser array using a rectangular model, in this and the previous section. The measured fields are analyzed in the following section.

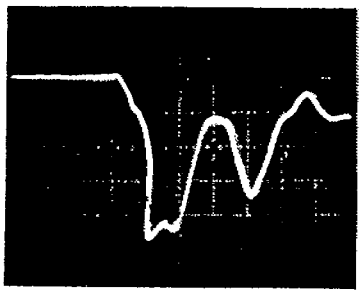

(a) POSITION A
2.5 T/s/DIV

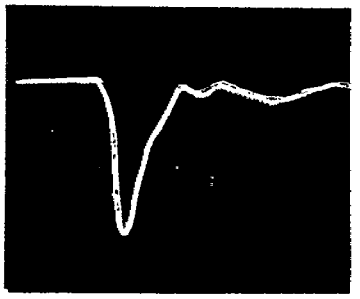

(d) POSITION D
10 T/s/DIV

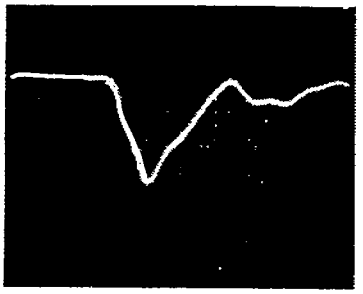

(b) POSITION B
5 T/s/DIV

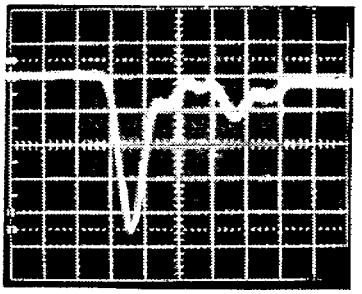

(e) POSITION E
5000 T/s/DIV

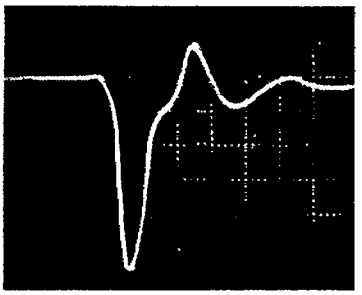

(c) POSITION C
5 T/s/DIV

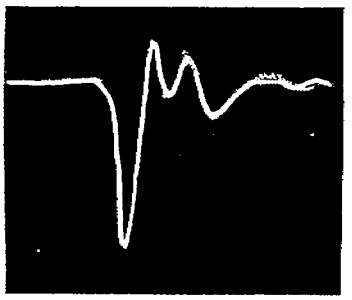

(f) POSITION F
5 T/s/DIV

SWEEP SPEED: 2 ns/DIV

Figure 28. $\dot{B}(t)$ measured in a staggered $(3 \times \dot{3})$ array with a simultaneous drive, using a TEK-109 (50 V, 250 ps) source.

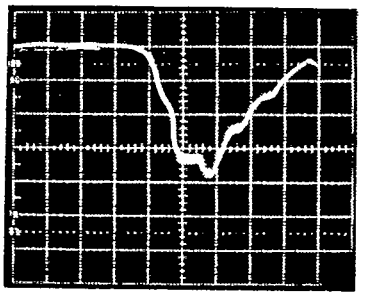

(a) POSITION A
5000 T/s/DIV

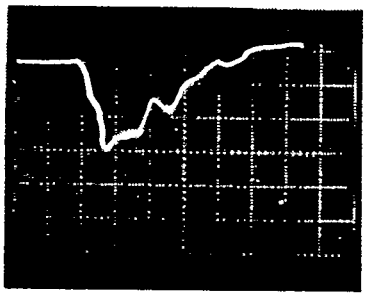

(d) POSITION D
10,000 T/s/DIV

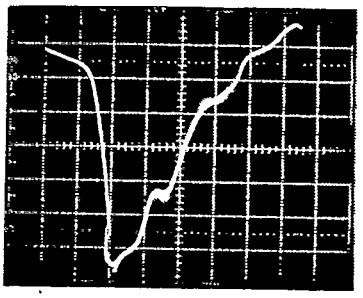

(b) POSITION B
2500 T/s/DIV

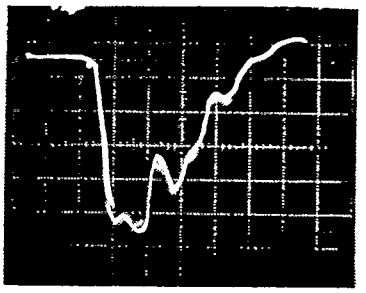

(e) POSITION E
2500 T/s/DIV

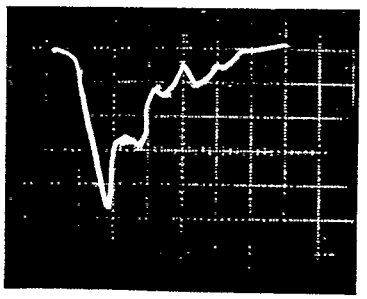

(c) POSITION C
5000 T/s/DIV

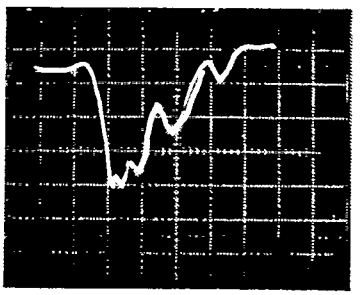

(f) POSITION F
2500 T/s/DIV

SWEEP SPEED: 5 ns/DIV

Figure 29. $\dot{B}(t)$ measured in a staggered (3 × 3) array with a simultaneous drive, using a Maxwell 40151 (50 KV, < 10 ns) source.

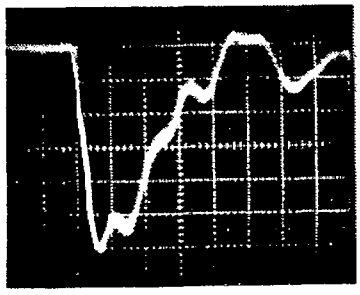

(a) POSITION A
2.5 T/s/DIV

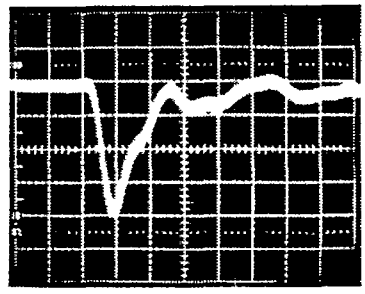

(d) POSITION D
10 T/s/DIV

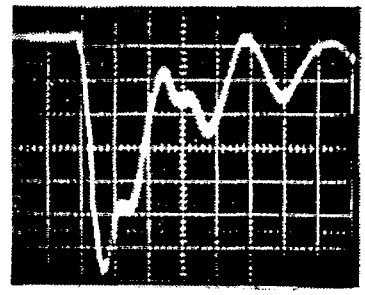

(g) POSITION G
2.5 T/s/DIV

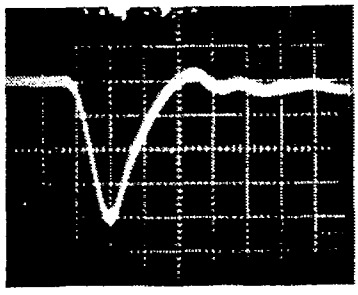

(b) POSITION B
5 T/s/DIV

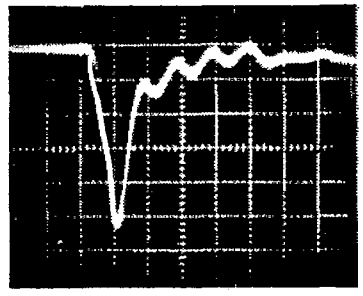

(e) POSITION E
5 T/s/DIV

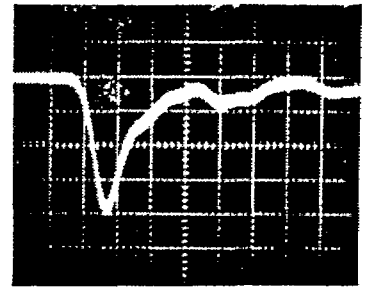

(h) POSITION H
5 T/s/DIV

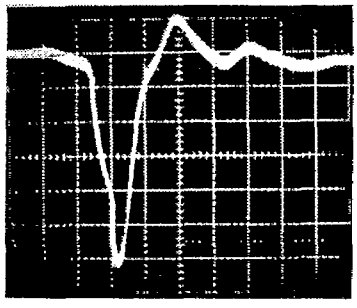

(c) POSITION C
5 T/s/DIV

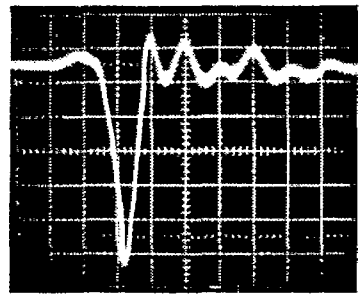

(f) POSITION F
5 T/s/DIV

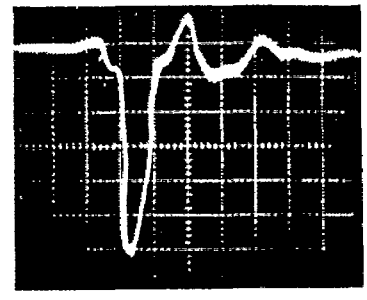

(i) POSITION I
5 T/s/DIV

SWEEP SPEED: 2 ns/DIV

Figure 30. $\dot{B}(t)$ measured in a staggered (3 × 3) array in a swept drive mode, using a TEK-109 (50 V, 250 ps) source.

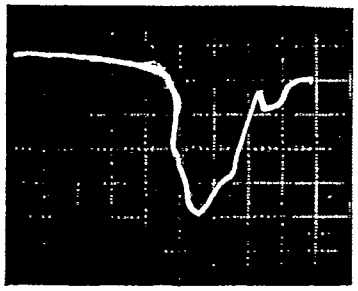

(a) POSITION A

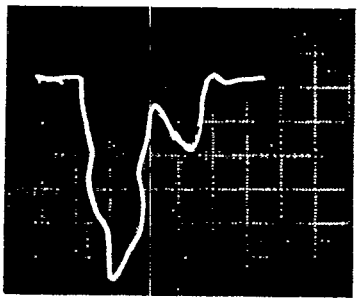

(d) POSITION D

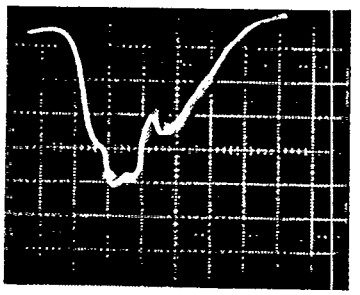

(g) POSITION G

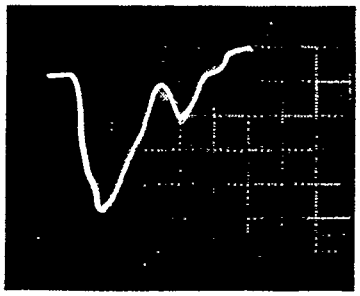

(b) POSITION B

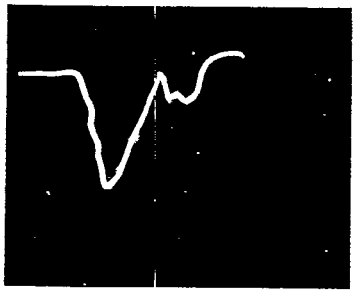

(e) POSITION E

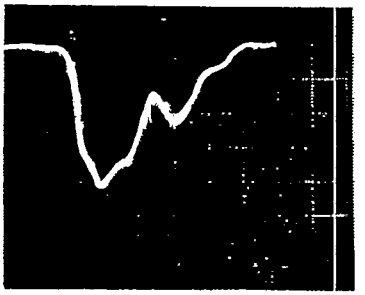

(h) POSITION H

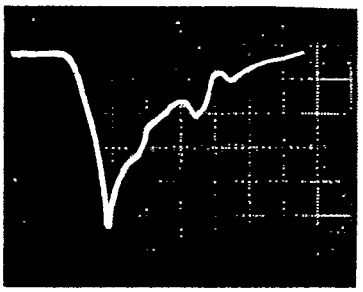

(c) POSITION C

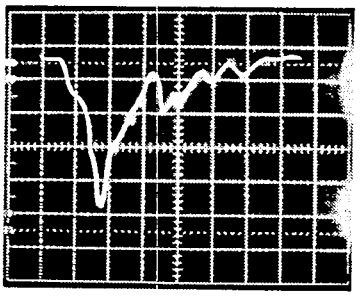

(f) POSITION F

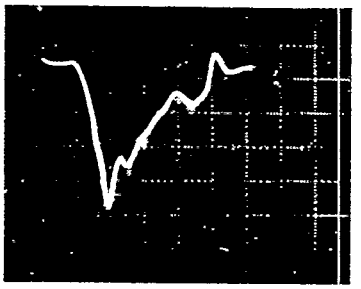

(i) POSITION I

SWEEP SPEED: 5 ns/DIV VERTICAL SCALE: 5000 T/s/DIV

Figure 31. $\dot{B}(t)$ measured in a staggered (3 × 3) array in a swept drive mode, using a Maxwell 40151 (50 KV, < 10 ns) source.

5. Analysis of the Experimental Data

One can look at the measured magnetic field data in terms of peak fields and the effective rise times τ_e as defined in (1). Basically, the interpretation and comparisons of the various measurements fall into two categories; a) comparing the rectangular and square rails for the peak fields and τ_e while they are driven by the same source and b) comparing the 3 × 3 pulser array configurations.

A. Rectangular (2:1) and square rails

In figures 32 and 33, we compare the peak field and τ_e for the rectangular and square rails, while each is driven by the same (100 KV, < 10 ns) pulse source. The comparisons are made at the four positions A, B, C and D, described in figure 5 for the rectangular rail and in figure 16 for the square rail. From figure 32, it is evident that the peak fields are higher for the square rails at all 4 positions, and by about 38% on an average. Note that the square rails are physically smaller and the current densities on the square rails are higher. Also, positions B and D are relatively farther from the "switch gap" in the rectangular case than in the square case. Similarly, τ_e, derived from an integration of $\dot{B}(t)$ (see (1)) is smaller for the square rail at all four positions measured.

B. 3 × 3 Array comparisons

It is noted that the 3 × 3 array of 9 pulsers has been configured in four different ways; (a) in-line simultaneous drive, (b) in-line swept drive, (c) staggered simultaneous drive and (d) staggered swept drive.

The peak magnetic fields, in each of the above four configurations measured with the Maxwell 40151 (50 KV, < 10 ns) source are shown in figure 34. One can observe that the staggered swept drive configuration leads to the highest values of fields in general. With regards to comparing the effective rise times τ_e, TEK-109 source which has a pulse rise time of the order of 250 ps is an appropriate driver, given that the transit time across the rail length of 1 m is of the order of 3 ns. The output amplitude of the TEK-109 being only 50 v in our experiments and then fanned out nine ways, results in a low B-dot signal levels. In this case, B-dot data is digitized and software integrated, while determining τ_e. A sample τ_e calculation is shown in the appendix later. The bar chart in figure 35 shows the values of τ_e at different positions, for the

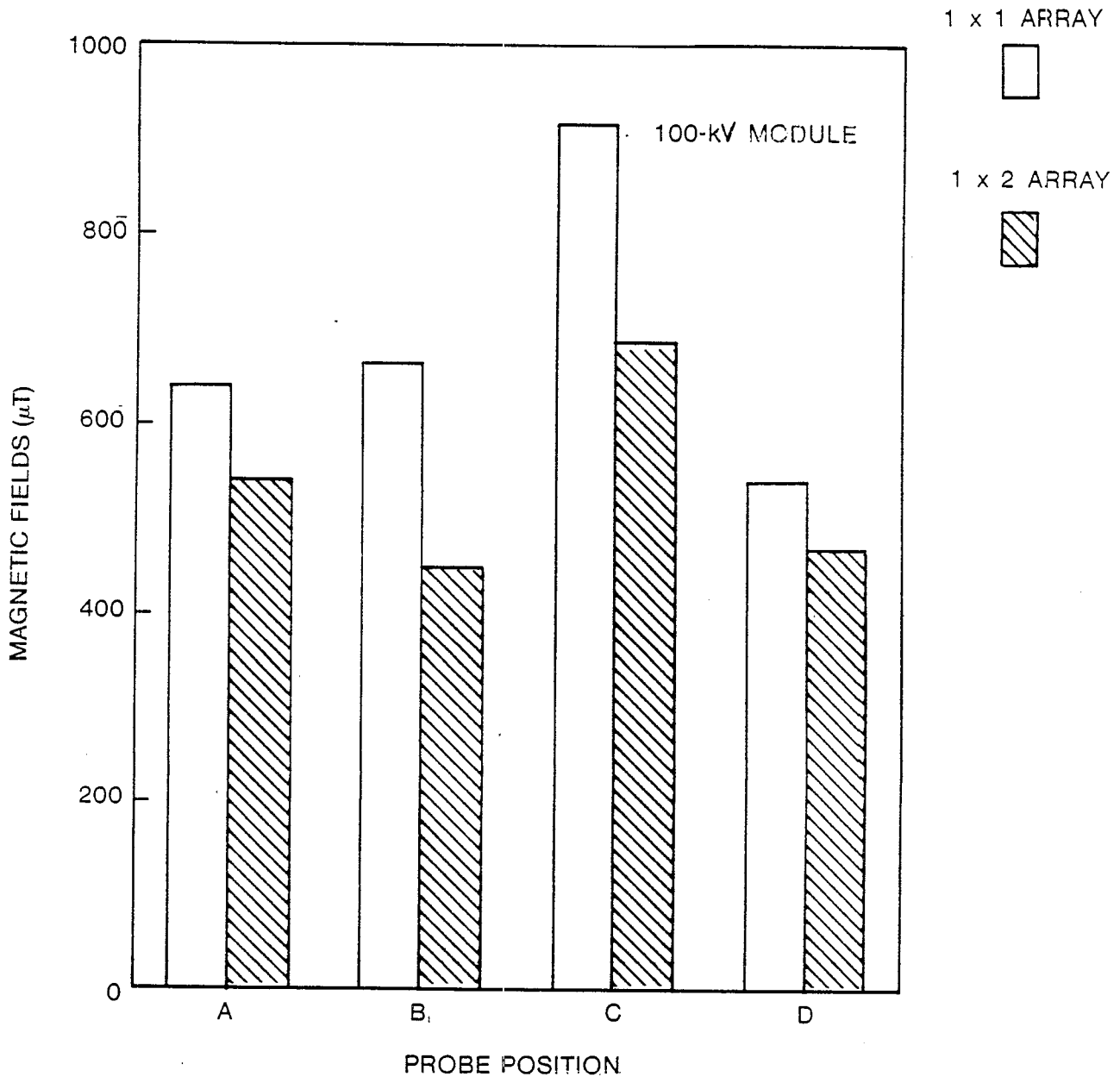

Figure 32. Peak magnetic fields at positions A, B, C and D for a rectangular (2:1) and a square rail driving a unit cell.

$T = \int \dot{B}\ dt/12\ ns/\dot{B}/pk$

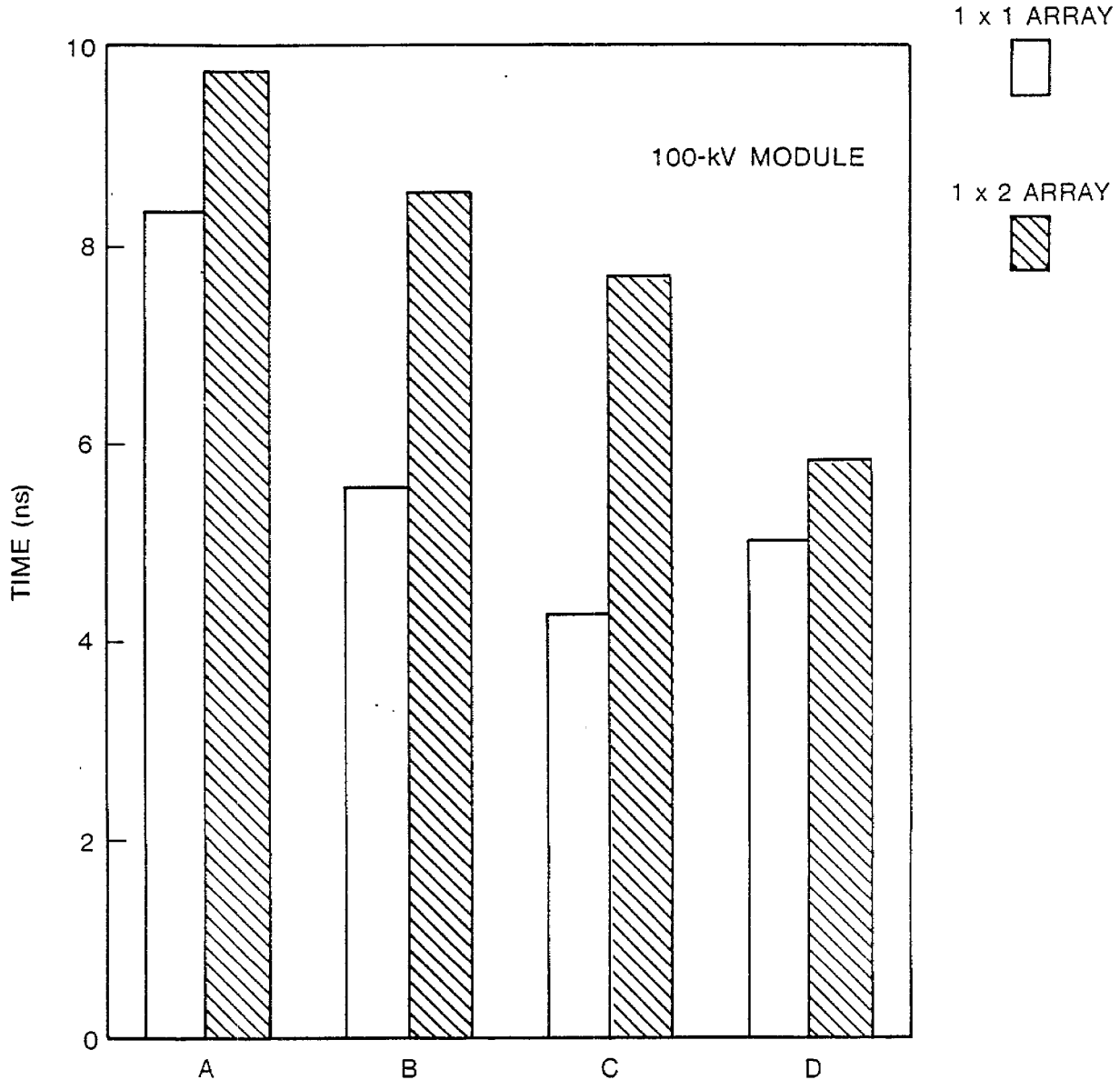

Figure 33. Measured τ_e at positions A, B, C and D for a rectangular (2:1) and a square rail driving a unit cell

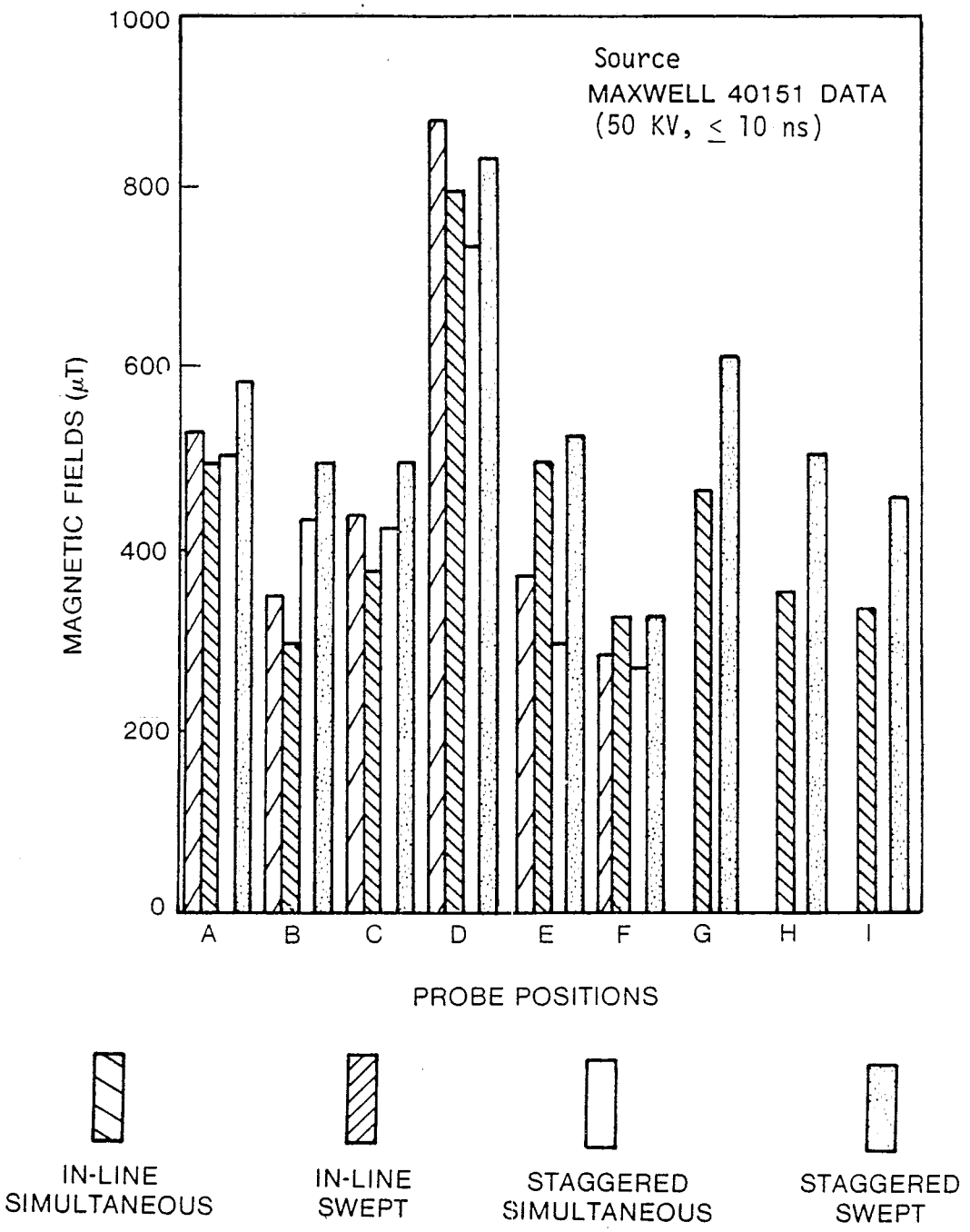

Figure 34. Peak magnetic field at various positions (see figures 21 and 22) for the 3 × 3 array configured in four different ways.

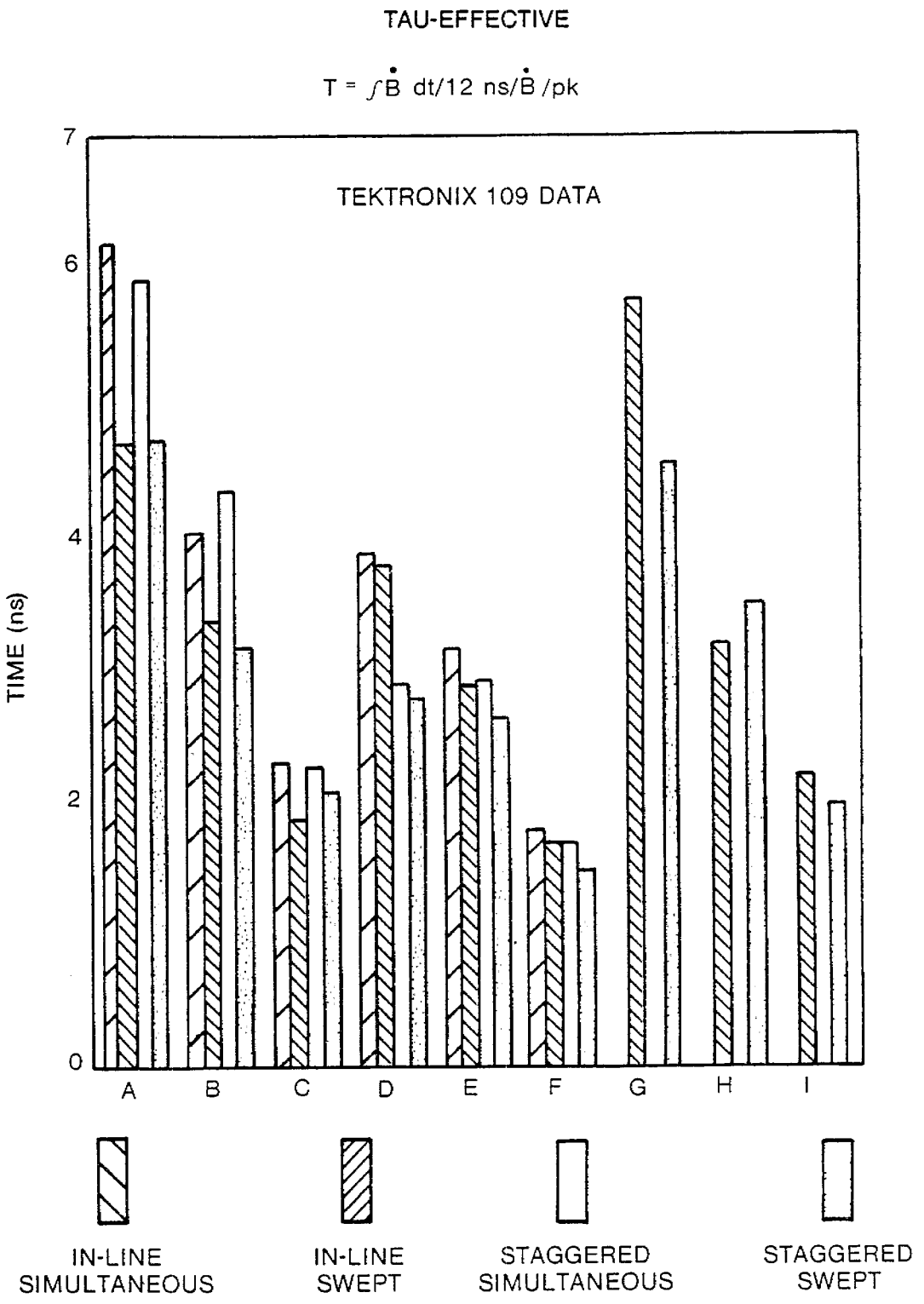

Figure 35. Measured τ_e at positions A to I (see figures 21 and 22) for the 3 × 3 array configured in four different ways.

four configurations of the 3 × 3 pulser array. Once again, it is seen that the staggered swept array has the best overall rise characteristics. The rise tane τ_e data of the bar chart in figure 34 is also displayed graphically in figure 36. The value of τ_e is indicated at the location where it is measured in figure 36.

It is observed that although the square rails produced slightly higher field strengths, the rectangular model was chosen for the 3 × 3 pulser array. For the same pulser voltage, as long as the switch inductance is low enough, it takes half the number of the rectangular rails to cover the same area, with a minor or no cost in terms of field strengths.

Further, in conclusion it may be stated that the staggered array is superior to an in-line array in terms of its rise characteristics or equivalently, the staggered array has an improved high frequency performance characteristics.

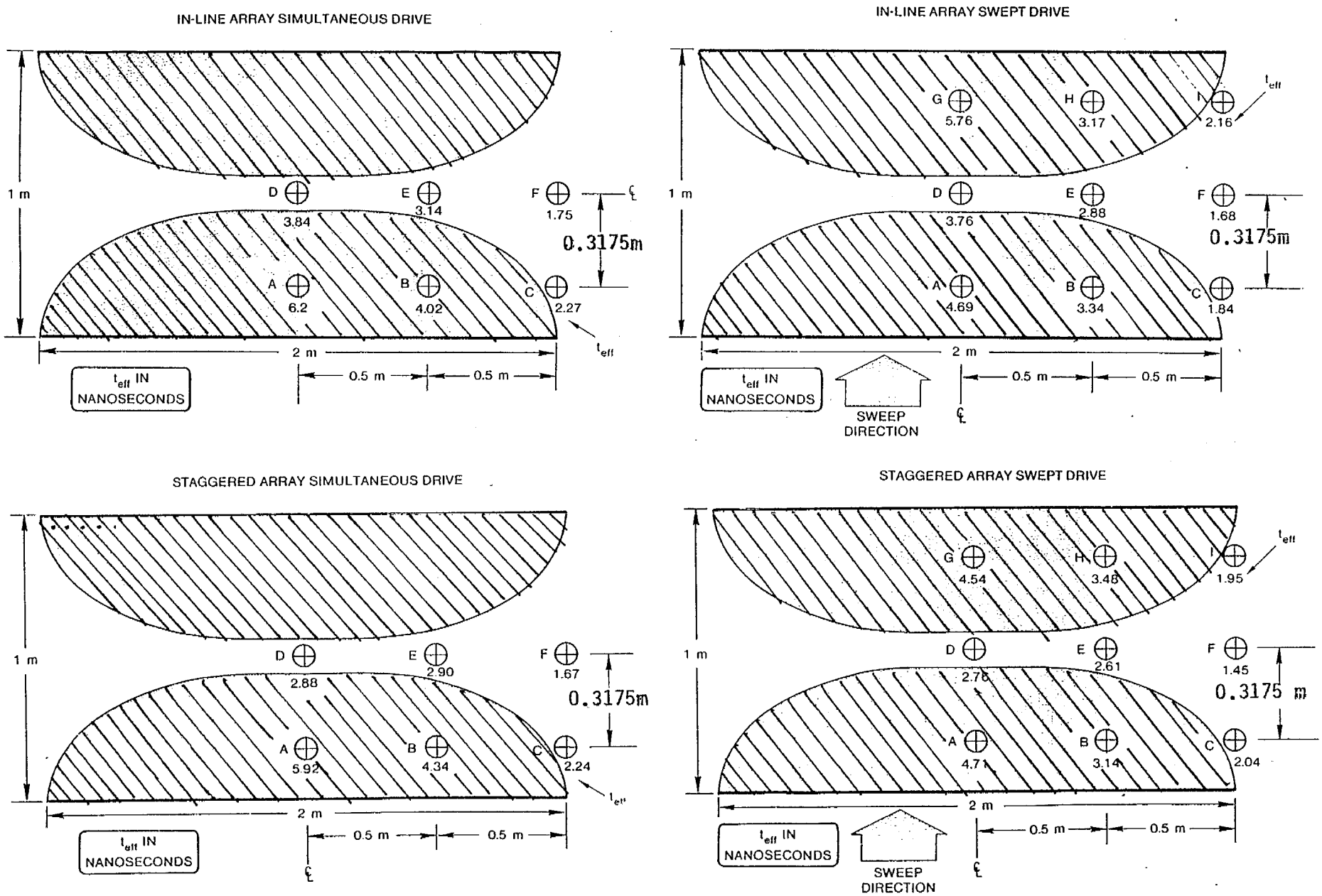

Figure 36. Measured τ_e at various positions in the 3 × 3 pulser array configurated in four different ways. (τ_e is indicated in ns at the measured locations).

6. Summary

If one wishes to drive electromagnetic fields into the ground, for whatever application, it can be done by a sheet source at the interface. This idealized sheet source can be simulated in practice by a two dimensional array of discrete sources at a height h above the interface. One then requires, suitably shaped conductors in getting from the pulser's switch gaps to the interface. The theoretical considerations of such conductors were considered by the authors in an earlier note [1] and in this note we have dealt with an experimental optimization of these conductors, called rails, in terms of their sizes and shapes. The rails have been optimized by considering a unit cell (i.e., one pulser with one pair of rails) and measuring the TDR. Rectangular and square rails have been considered and various experimental parameters varied during rail optimization. Rectangular rails (6m × 3m) with a 2:1 aspect ratio, illuminates twice the area of a square rail (3m × 3m) and still produce field strengths that were about 20% lower than the square rail model. Later an array of 9 unit cells (3 × 3) were fabricated using a rectangular (2:1) rail model that use the optimized rail configuration from the TDR data. Field measurements were made for the 3 × 3 array arranged in both in-line and staggered configurations. Each of these arrangements can also be excited in a simultaneous or a swept mode. The measured $\dot{B}(t)$ are reported along with the derived B(t). An effective rise time $\tau_e = B_{peak}/\dot{B}_{peak}$ is computed in each case. The array configurations are compared for both peak fields and τ_e. Staggered arrays are found to exhibit better high frequency performance characteristics.

In conclusion, it is observed that an efficient way of coupling fields into ground, (in general a lossy dielectric) has been demonstrated both theoretically and experimentally, for possible applications in the future.

APPENDIX-1

Experimental Procedures

The magnetic field probe used in these measurements is the MGL-6A (A) with an equivalent area of $10^{-3} m^2$. Two equal lengths of RG-402 cables connect the output fromthe sensor to a screen box. The recording system is shown as a block diagram in figure A.1. The screen box is located 2 m from the end of the test-unit cell and on its central line. This box itself is electrically "floating" while containing an oscilloscope (type Tektronix 485) with a camera and a battery power pack. The signals from the MGL-6A (A) sensor are recorded differentially (A-B). While monitoring the surface magnetic field, the sensor cables produce a voltage signal V(t) related to a certain component of the magnetic flux density $\vec{B}(\vec{r},t)$ via.

$$V(\vec{r},t) = A_{eq} \frac{dB}{dt} (\vec{r},t) \qquad (A.1)$$

with A_{eq} being the equivalent area of the sensor (= $10^{-3} m^2$ for the present case). The scope signal is integrated with an RC passive integrator of time constant 1 μs, and in some cases the derivative data is digitized and numerically integrated using a computer. Examples of $\dot{B}(t)$ and B(t) are shown in figures A-2 and A-3. From the data in these figures an effective rise time τ_e is computed using

$$\tau_e = \frac{B(t)_{peak}}{\dot{B}(t)_{peak}} \qquad (A.2)$$

Since in most cases the peak value of B(t) was unattainable, we have consistently used B(t = 12 ns) as the "peak" value. Consequently, the τ_e values, while not absolute, are useful in relative comparisons as they give us a number that is proportional to the rise time. Sample calculations of τ_e are shown in figures A-2 and A-3.

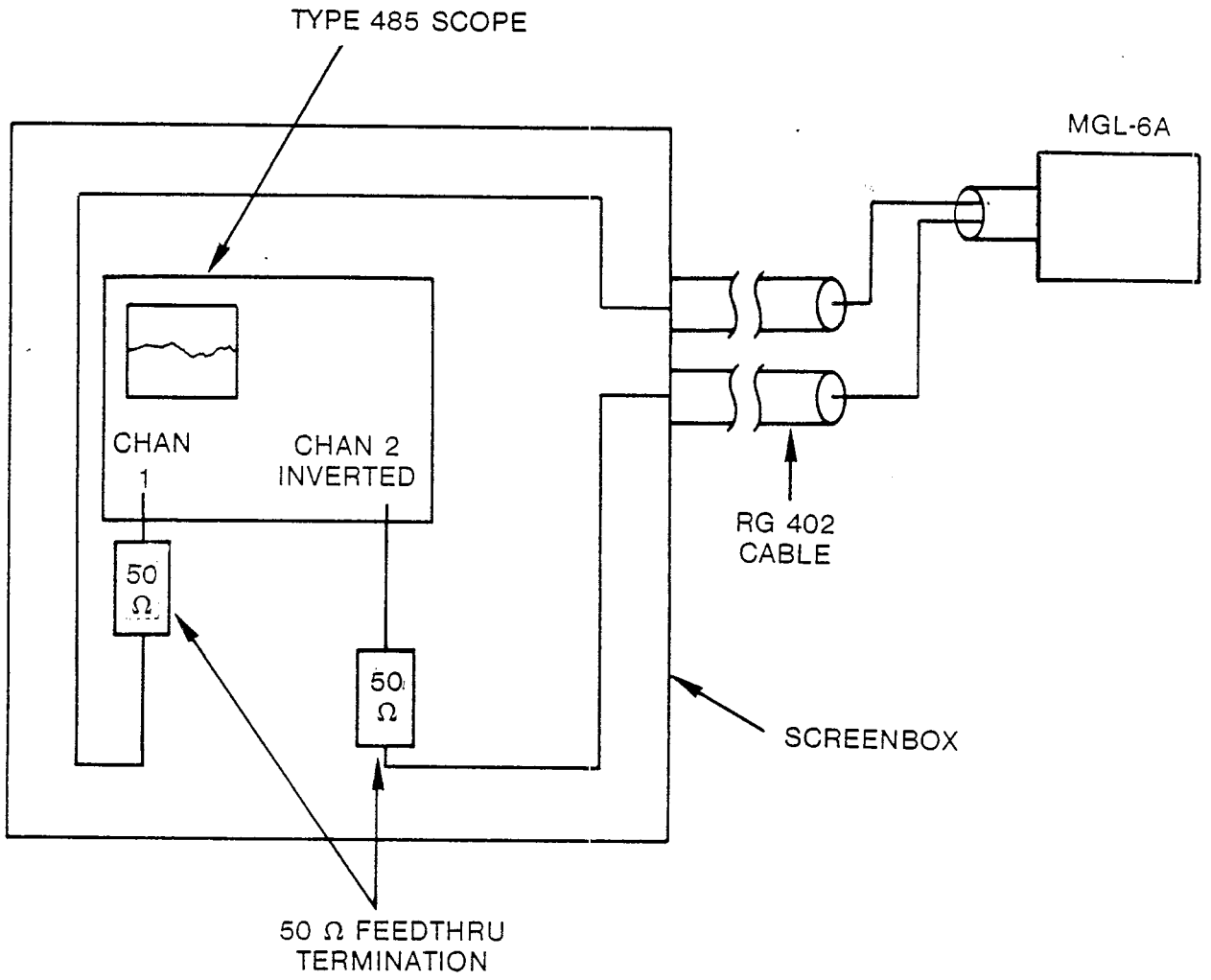

Figure A-1. Block diagram of the recording system.

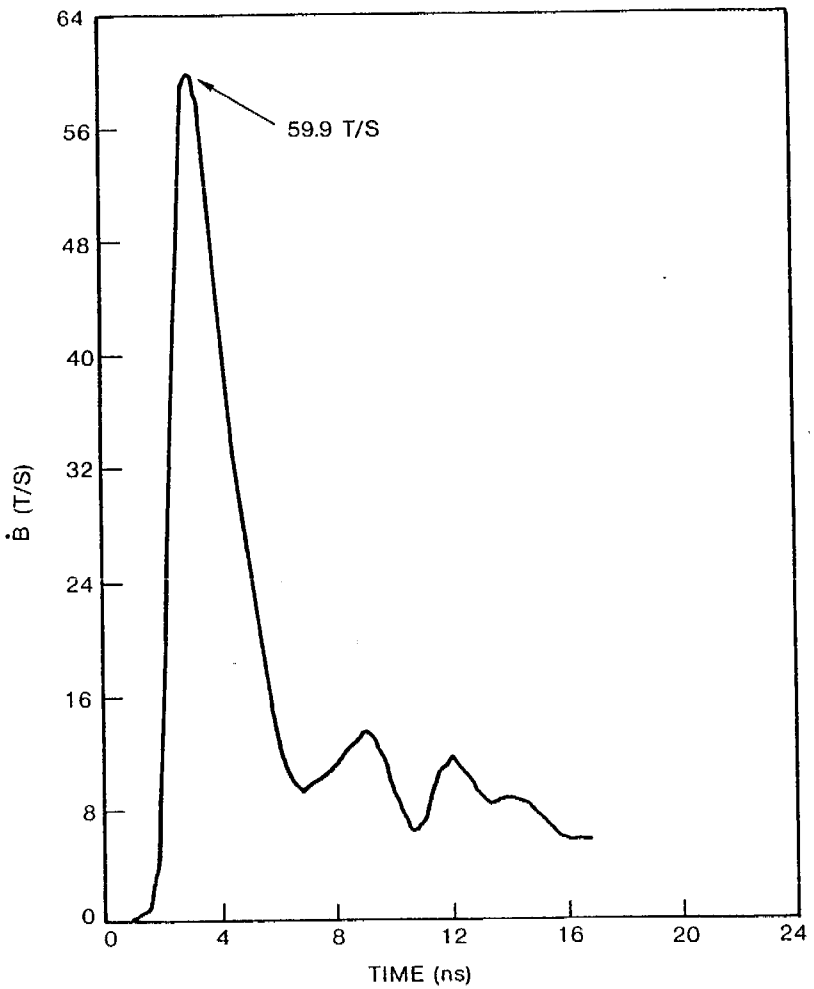

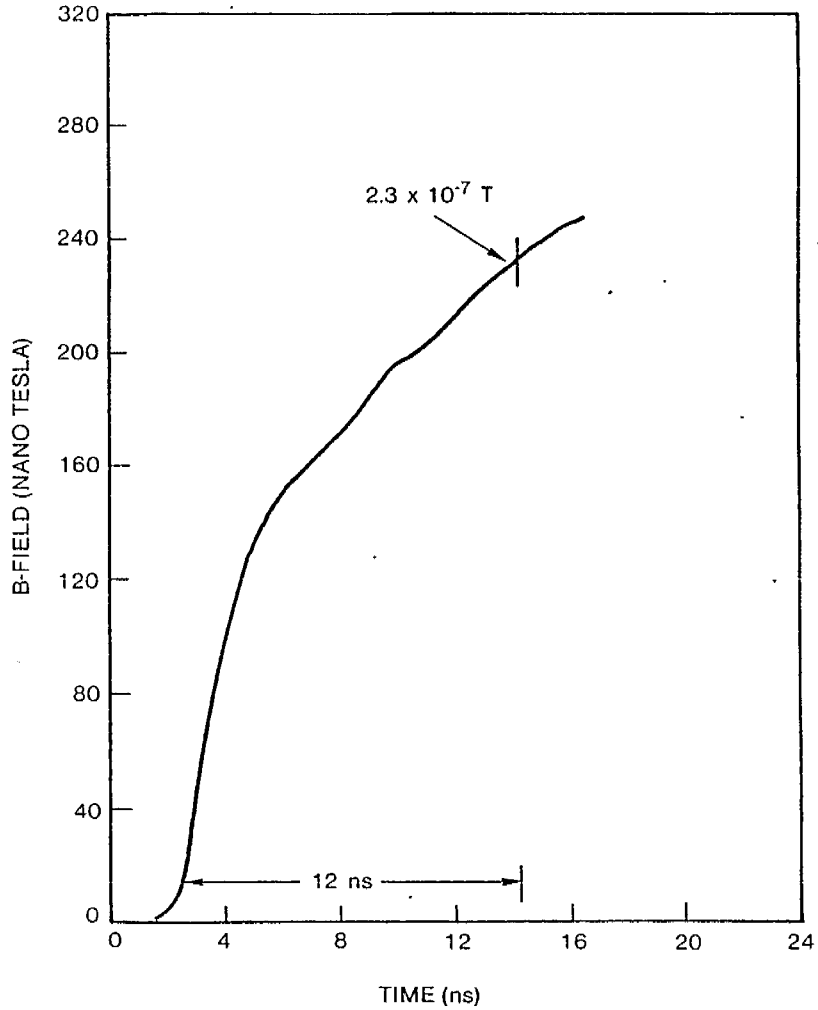

Figure A-2. $\dot{B}(t)$ and $B(t)$ for an in-line simultaneous 3×3 array.

NOTE: $\tau_e \simeq (2.3 \quad 10^{-7}/59.9) \simeq 3.84$ ns

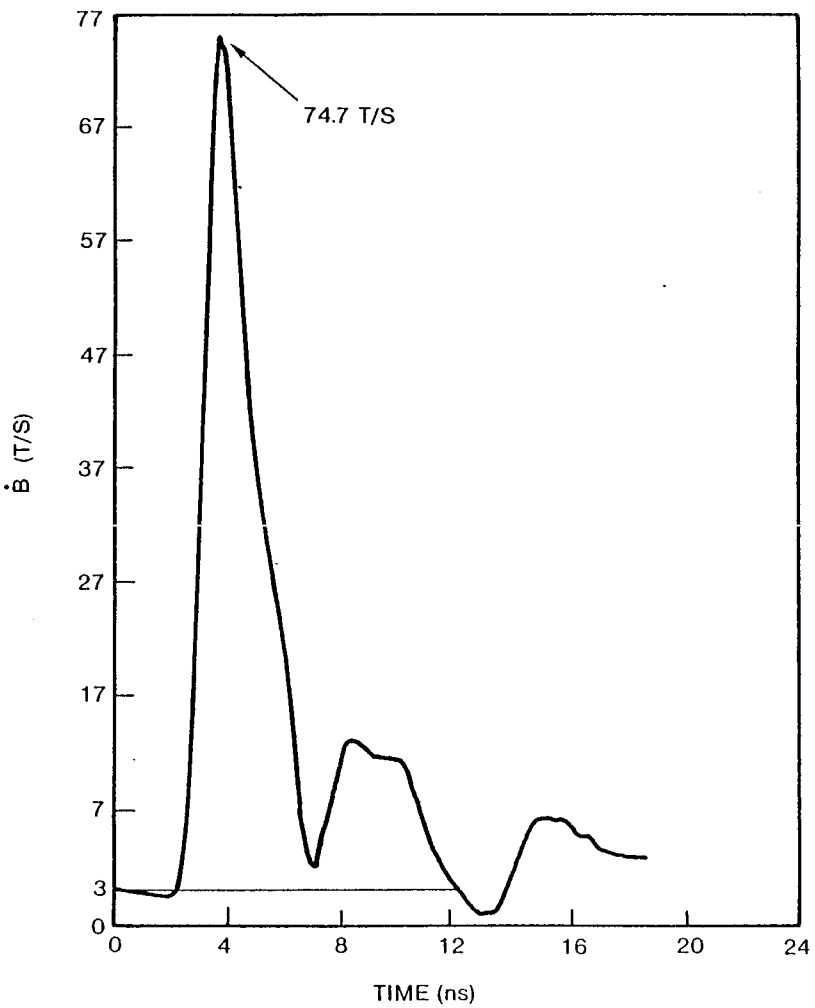

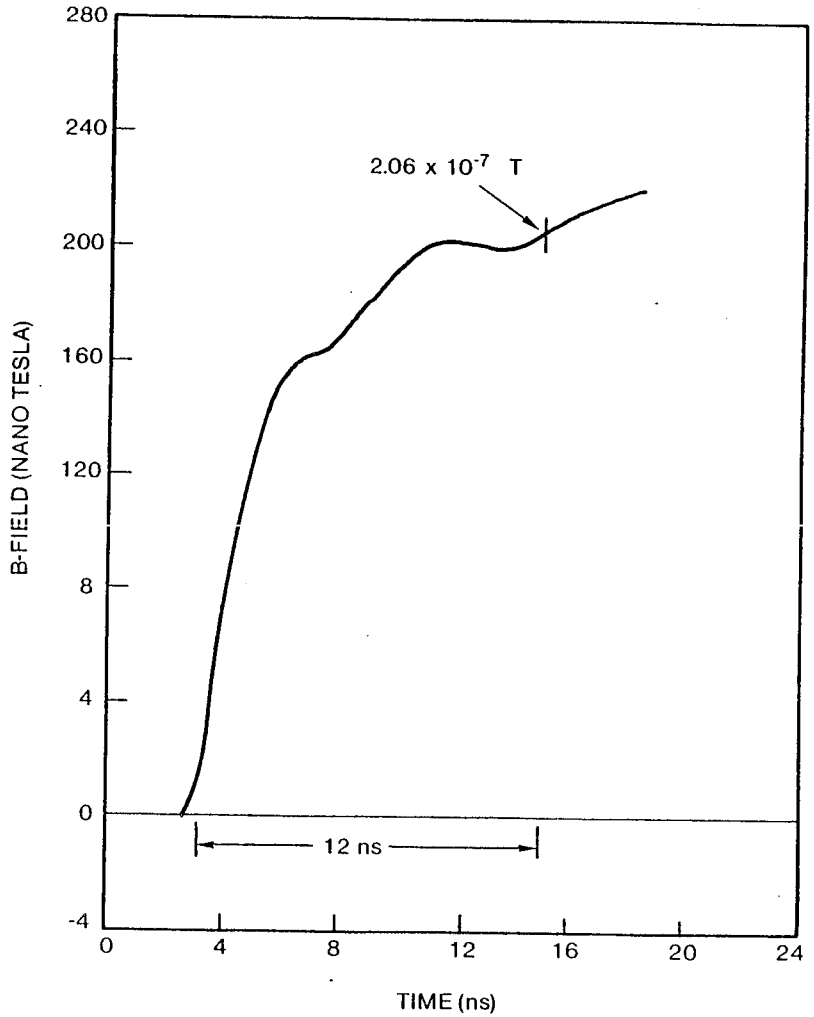

Figure A-3. $\dot{B}(t)$ and $B(t)$ for a staggered, swept 3×3 array.

NOTE: $\tau_e \simeq (2.06 \times 10^{-7}/74.7) \simeq 2.76$ ns.

References

[1] Y. G. Chen, S. Lloyd, R. Crumley, C. E. Baum, and D. V. Giri, Design Procedures for Arrays Which Approximate a Distributed Source at the Air-Earth Interface," Sensor and Simulation Note 292, 1 May 1986.

[2] C. E. Baum, "EMP Simulators for Various Types of Nuclear EMP Environments: An Interim Categorization," Sensor and Simulation Note 240, January 1978 and Joint Special Issue on the Nuclear Electromagnetic Pulse, IEEE Trans. on Antennas and Propagation, January 1978, pp. 35-53, also in the Special Issue on the Nuclear Electromagnetic Pulse, IEEE Trans. on Electromagnetic Compatibility, February 1978, pp. 35-53.

[3] C. E. Baum, "The Brewster Angle Wave Matcher," Sensor and Simulation Note 37, 13 March 1967.

[4] C. E. Baum, "The Planar, Uniform Surface Transmission Line Driven from a Sheet Source," Sensor and Simulation Note 48, 10 August 1967.

[5] C. E. Baum, "A Simplified Two-Dimensional Model for the Fields Above the Distributed-Source Surface Transmission LIne," Sensor and Simulation Note 66, 20 December 1968.

[6] C. E. Baum, "A Distributed Source Conducting-Medium Simulator for Near and Below the Ground Surface," Sensor and Simulation Note 87, 9 July 1969.

[7] F. C. Yang, "A Distributed Source-Region EMP Simulator," Sensor and Simulation Note 266, July 1980.

[8] Y. G. Chen, R. Crumley, S. Lloyd, C. E. Baum, and D. V. Giri, "Lumped Element Networks for Replacing Sections of a Buried Transmission Line," Sensor and Simulation Note 288, 12 September 1985. also published in IEEE Trans. on Electromagnetic Compatibility, Vol.30, No.4, November 1988, pp 449-456.

[9] Y.G.Chen, S.Lloyd, R.Crumley, C.E.Baum and D.V.Giri, "Surface-Current-Density Measurements via Apertures," Sensor and Simulation Note 290, 14 October 1985, also published in the Conference Record of the Workshop on Measurements of Electrical Quantities in Pulse Power Systems II held at National Bureau of Standards, Gaithersburg, MD., March 5-7, 1986.

[10] T.M.Flanagan, C.E.Mallon, R.Denson, R.Leadon and C.E.Baum, "A Wide-Bandwi Electric-Field Sensor for Lossy Media, " Sensor and Simulation Note 297, 30 January 1987.